Journal of The Electrochemical Society

The Electrochemical Society
Advancing solid state & electrochemical science & technology

Modeling of Chemo-Mechanical Multi-Particle Interactions in Composite Electrodes for Liquid and Solid-State Li-Ion Batteries

To cite this article: Donald Bistri and Claudio V. Di Leo 2021 *J. Electrochem. Soc.* **168** 030515

Journal of The Electrochemical Society, 2021 **168** 030515
1945-7111/2021/168(3)/030515/23/$40.00 © 2021 The Electrochemical Society (“ECS”). Published on behalf of ECS by IOP Publishing Limited

Modeling of Chemo-Mechanical Multi-Particle Interactions in Composite Electrodes for Liquid and Solid-State Li-Ion Batteries

Donald Bistri and Claudio V. Di Leo[z]

School of Aerospace Engineering, Georgia Institute of Technology, Atlanta, GA 30332, United States of America

Modeling of the chemo-mechanical interactions between active particles in battery electrodes remains a largely unexplored research avenue. Of particular importance is modeling the local current densities which may vary across the surface of active particles under galvanostatic charging conditions. These depend on the local, stress-coupled electrochemical potential and may also be affected by mechanical degradation. In this work, we formulate and numerically implement a constitutive framework, which captures the complex chemo-mechanical multi-particle interactions in electrode microstructures, including the potential for mechanical degradation. A novel chemo-mechanical surface element is developed to capture the local non-linear reaction kinetics and concurrent potential for mechanical degradation. We specialize the proposed element to model the electrochemical behavior of two electrode designs of engineering relevance. First, we model a traditional liquid Li-ion battery electrode with a focus on chemical interactions. Second, we model a next generation all-solid-state composite cathode where mechanical interactions are particularly important. In modeling these electrodes, we demonstrate the manner in which the proposed simulation capability may be used to determine optimized electro-chemical and mechanical properties as well as the layout of the electrode microstructure, with a focus on minimizing mechanical degradation and improving electrochemical performance.

[DOI: 10.1149/1945-7111/abe8ea]

Manuscript submitted December 7, 2020; revised manuscript received February 4, 2021. Published March 8, 2021.

Supplementary material for this article is available online

Lithium ion batteries (LIBs) have become the dominant energy storage source in a number of areas including consumer electronics and electric vehicles.[1] A number of research avenues exist for the continued improvement of LIBs including improved charging times, increased operational lifespan, expanded capacity, and improved safety.[2,3] In pursuit of these improvements, research has been shifting from conventional liquid LIBs towards next generation all-solid-state battery (SSB) architectures with enhanced current densities ($\approx$3860 mAh g^{-1}), wider electrochemical window (0–5 V), and improved safety.[4–8] However, battery designs, be it for conventional liquid LIBs or next-generation SSBs, suffer from inherent mechanical degradation across different cell constituents, which in turn limit their electrochemical performance. Upon intercalation/de-intercalation of lithium ions, current electrode designs undergo large inhomogeneous volumetric changes, which give rise to large mechanical stresses and inelastic effects.[9–12] This in turn can lead to mechanical degradation, which for example may take the form of fracture of the individual constituents or debonding of active materials from their surrounding matrix, as has been reported in the literature.[13–17] The role of mechanical stresses and mechanical degradation on electrochemical performance is even more critical in all-solid-state architectures owing to the presence of a stiff solid electrolyte. Aside from conventional fracture mechanisms at the electrode level,[18–20] inherent mechanical instabilities associated with: i) metal filament growth,[21–23] and ii) interphase formation and interphase induced fracture of the solid-state electrolyte[24,25] have hindered commercialization of next generation SSB battery architectures.

Research to date on the coupling between mechanical degradation and electrochemical performance remains mostly limited to studying single-particle systems (cf.[14,26]). As such, our understanding of the role of mechanical degradation on electrochemical performance, including the effect of mechanics on interfacial kinetics, remains rather limited. From both an experimental and modeling perspective, it is thus critical to understand the complex interplay of mechanical deformation and chemical processes. This is particularly critical in the context of densely-packed microstructures traditionally employed in the design of composite electrodes for commercial batteries. Conventional composite electrode architectures build upon a compact conglomerate of active particles confined on their exterior by a matrix supporting percolation pathways for ionic conduction in addition to complementary additives for electronic conduction.[27–29] Owing to their compact nature, composite electrodes experience a complex interplay of chemo-mechanical interactions as lithium ions are inserted/extracted from the active particles, thus leading to the emergence of a complex stress field as the particles swell/deswell against the confining matrix. In addition to the mechanical behavior, there are concurrent electrochemical processes as local currents vary between particles in the composite electrode. From a modeling perspective, there is a need to capture multi-particle interactions—both mechanical and chemical—for these densely packed architectures in order to understand how variations in material properties and microstructure composition affect mechanical degradation and ultimately electrochemical performance.

Significant research efforts have been undertaken from a theoretical/computational perspective on understanding the chemo-mechanical behavior of single active particles, cf. Zhao et al.[30] Modeling frameworks have been developed to different levels of complexity for both intercalation electrodes with deformations usually confined within the elastic regime[31–36] and conversion electrodes undergoing volumetric strains in the order of more than 100% and experiencing large elastic-plastic deformations.[37–39] Theories coupling large elastic-plastic deformations with large volumetric swelling due to lithium diffusion have been formulated.[12,40–42] Specialization of the aforementioned theories has been extensively applied to capture the chemo-mechanical behavior of single Si-particles upon lithiation. For example, Zhao et al. developed a model of co-evolving plasticity and reaction upon lithiation of spherical, crystalline silicone (c-Si) particles in LIBs.[43] These theoretical frameworks have also been applied to capture the experimentally measured electrochemical response. Following a combination of experimental measurements and numerical simulations in a Li-ion half cell, Bucci et al.[44] adopted the theory of Bower et al.[40] to characterize the behavior of amorphous, thin film Si electrodes. The effect of elastic-plastic deformation on electrochemical performance of geometrically complex a-Si anodes experimentally realized by Wu et al.[45] was investigated in the work of Di Leo et al.[39]

While much has been done from a theoretical standpoint to model the chemo-mechanical behavior of single-particle systems, few studies have considered the combined multi-particle behavior of composite electrodes. In modeling the multi-particle behavior of

[z] E-mail: cvdileo@gatech.edu

electrodes, one can consider both mechanical and chemical interactions which occur between particles. Mechanical interactions arise from transfer of forces between particles either through direct particle-to-particle contact or through contact with the surrounding matrix. Early modeling efforts aimed at capturing mechanical interactions between active particles in electrodes centered on applications to traditional liquid LIBs. Experimentally, Lee et al.[46] studied mechanical interactions in Si-nanopillars using both in situ and ex situ characterization techniques to explore how mechanical interactions among neighboring nanopillars impacted reaction kinetics and their susceptibility to fracture upon lithiation. Numerical, finite-element simulations of a 2D, porous graphite/binder electrode microstructure were performed by Rahani et al.[47] to capture mechanical interactions between active particles and PVDF binders. In a similar effort, Higa and Srinivasan[48] investigated the role of both particle size and binder stiffness on the stresses induced in active particles, reporting a decrease in stress with decrease in particle size and binder stiffness. Garcia et al.[49] modeled 2D, porous electrodes of $Li_xMn_2O_4$ spherical particles under a linear-elastic finite-element framework. From a design standpoint, the effect of both packing density and particle size were considered. Microstructure configurations with dense particle aggregates were assessed to be detrimental to electrochemical performance, lowering the utilization of active material and leading to higher mechanical stresses induced in the particles.

Recently, numerical simulations of 3D reconstructed composite electrode microstructures under a continuum framework were performed by Zhao and co-workers.[27,28] The interplay between mechanical stresses and Li-ion diffusion was explored to quantify its role on capacity for two representative microstructures including: i) an NMC cathode undergoing small volumetric changes upon Li insertion, and ii) an SnO anode where volumetric changes upon lithiation are more significant. These simulations were later expanded by the same group to model damage both at the particle level and particle interface in NMC composite cathodes.[50,51] Efforts of a similar nature are also reported by Hoffman and co-workers,[52] where stochastic microstructure models were used for representatives of graphite anodes. While these works represent a step towards modeling of complex chemo-mechanical interactions in composite electrodes, development of a general computational framework, along with a suitable numerical implementation, capable of capturing appropriate galvanostatic charging conditions remains at its infancy and will be addressed in this work. Of interest here is thus the development of a general computational framework, which captures the role of local variations in chemo-mechanical properties and microstructure composition on the mechanical integrity and electrochemical performance of different electrode microstructures.

Within the context of all-solid-state batteries, the most notable efforts in modeling of composite electrodes—with a focus on the role of mechanics—are by Bucci and co-workers.[18–20] In Bucci et al.,[18] a joint analytical and finite-element framework is reported to model the effect of stresses in Silicon active particles within an SSE composite cathode. Here, particle size distribution and placement across the electrode domain were generated from a centroidal Voronoi tessellation. A critical Silicone to SSE volume fraction was reported above which mechanical stresses due to multi-particle interactions have a dominant effect on electrochemical performance and one is under-utilizing the added active material from a capacity standpoint. This work was subsequently extended to account for mechanical damage through use of cohesive elements both at the active particle-electrolyte interface[19] and the SSE itself.[20] Interestingly, compliant electrolytes were assessed to be more prone to micro-cracking. Additionally, fracture initiation at the active particle-SSE interface was reported for most combinations of SSE material properties, provided the active particles undergo 7.5% change in volume upon lithiation. From a design standpoint, the authors also determined that initiation of fracture occurred regardless of the size of active particle, making the claim that nanostructured electrodes need not perform better from a mechanical standpoint. In the context of all-solid-state batteries, the role of mechanical interactions on transport properties has been recently explored in the work of Behrou and Maute.[53] Here, the effect of damage on mechanical behavior and effective transport properties was studied using a non-local damage model with both mechanical stiffness and diffusivity of active particles penalized with damage evolution. In the same spirit, the role of mechanics on effective transport properties and electrochemical performance of SSBs with increase in active material was also investigated in the work of Al Siraj et al.[54] A critical active material volume fraction was determined above which electrochemical performance does not increase as conduction pathways are significantly decreased.

While research efforts have been devoted to capturing mechanical interactions at the electrode microstructure, modeling of the concurrent *chemical interactions between active* particles arising from diffusion of Li-ions through the electrolyte remains largely unexplored. An inherent obstacle in modeling of chemical interactions between particles is implementation of true galvanostatic conditions. During galvanostatic charging, the total current over all particles is held constant, but the individual current distributions at each particle surface are unconstrained and depend on the local, stress-coupled, non-linear reaction kinetics.

In this work, we formulate and numerically implement a theoretical framework based on the use of a chemo-mechanical interface element, analogous in form to conventional cohesive elements used in fracture mechanics, to model the stress-coupled, non-linear kinetics of ionic transport at the particle/electrolyte interface. We deploy this new element to model galvanostatic charging of composite electrodes and study their electrochemical performance. The proposed interface element is introduced at the surface of active particles within the numerically discretized composite electrode microstructures to capture the non-linear, stress-coupled, reaction kinetics. Further, mechanical degradation of the interface is concurrently modeled—accounting for a loss in reactivity due to damage—to assess the interplay of mechanical stresses and damage on the behavior of the microstructure. In this work, we investigate the chemo-mechanical behavior of various composite electrodes under galvanostatic charging with a focus on understanding how microstructural features such as particle size distribution, packing density, and local material properties affect the overall electrochemical behavior of the microstructure. First, we focus on pure electrochemical particle-particle interactions by modeling a representative liquid LIB electrode composed of an ensemble of hollow, double-walled Si nanotubes,[45] whose chemo-mechanical behavior has been previously studied for a single active nanotube. Second, we focus on a $LiCoO_2$-$Li_{10}GeP_2S_{12}$ (LCO-LGPS) composite cathode for next-generation SSBs in which both mechanical and electrochemical multi-particle interactions are relevant due to the presence of a relatively stiff SSE matrix.

The paper is organized as follows. First, the theoretical and numerical framework is detailed in section "Theoretical and Numerical Framework". This section details the continuum description of a representative volume element (RVE) of the microstructure , followed by a detailed description of the constitutive modeling and numerical discretization of the individual particles and of the interfaces. We demonstrate the capabilities of our numerical framework in the section titled "Numerical Framework Demonstration" through a simple example of a two-particle electrode RVE. In the two following sections we apply our numerical framework to model experimentally relevant electrode microstructures. First, we investigate a traditional liquid LIB electrode design composed of multiple double-walled hollow nanotubes. Here, only chemical interactions between the multiple active particles are considered and we explore the role of material properties and interfacial damage on electrode performance. Second, we model a representative solid-state composite cathode where mechanical load transfer through the SSE is significant. Here, we study both the role of varying material properties, and the role of varying microstructural descriptors such as particle size and packing density. We summarize our observations in the final section and conclude with potential avenues for future research.

Theoretical and Numerical Framework

We describe the multi-particle behavior of a composite electrode by considering various scales. We first consider a representative volume element (RVE) of the microstructure through a continuum description and subsequently we focus on the behavior of individual active particles and finally transition to the behavior of the interfaces. This description is shown schematically in Fig. 1 with a focus on the treatment of the electrochemical behavior.

Continuum microstructural RVE description.—We consider first the continuum behavior of a representative volume element (RVE) of the microstructure as shown in Fig. 1a. A critical aspect of capturing the electro-chemo-mechanical behavior of this microstructure is proper implementation of galvanostatic charging conditions. Here, total current I over the entire domain is held constant, while current density over a particular particle, $i^{(k)}$, is free to fluctuate across the particle surface. To ensure galvanostatic charging conditions we must enforce

$$I = \sum_{k=1}^{N} I^{(k)}, \quad \text{with} \quad I^{(k)} = \int_{A^{(k)}} i^{(k)} dA \tag{1}$$

where N is the number of particles in the RVE. Equation 1 serves as a constraint, which must be numerically enforced over the entire simulation domain. We assume from the onset *that voltage across all particle surfaces is constant*. We thus restrict ourselves to physical problems in which Ion diffusion through the matrix is sufficiently fast and variations in electric potential through the electrolyte are negligible, which ensure a constant voltage across the microstructure RVE. From a numerical perspective, this has the added benefit that we may exclusively focus on the interfacial kinetics and active particle behavior without having to resolve ion migration and the associated electric field. We note that the proposed numerical framework may be expanded to remove the constraint that the voltage be a constant across all particle surfaces by concurrently modeling transport of ionic species across the electrolyte, namely the physics of Ion migration and species diffusion. The development presented here is a simplification of this more general case, but should serve equally useful in the development of future models which include this additional physics.

To model non-equilibrium interface reaction kinetics, we employ the phenomenological Butler-Volmer equation. At every point on the surface of a particle, current density i is related to the overpotential η through (cf. Bazant[55])

$$i = i_0(\bar{c})\left(\exp\left(-\frac{\alpha F\eta}{R\vartheta}\right) - \exp\left(\frac{(1-\alpha)F\eta}{R\vartheta}\right)\right). \tag{2}$$

Here $i_0(\bar{c})$ is the concentration dependent exchange current density, R the gas constant, ϑ the absolute temperature, F the Faraday constant, and α is a symmetry factor, representative of the fraction of surface overpotential promoting anodic or cathodic reaction at the electrode interface, constrained by $0 < \alpha < 1$. The exchange current density depends on species concentration through

$$i_0(\bar{c}) = Fk_0(1-\bar{c})^{\alpha}\bar{c}^{(1-\alpha)}, \tag{3}$$

where k_0 is the reaction constant and $\bar{c}$ is a normalized concentration detailed in a subsequent section. From thermodynamics, we may relate the overpotential, η, to the difference in electrochemical potential of the reactants and products of the reaction at the electrode-electrolyte interface, $\Delta\mu$, through

$$\eta = (\phi^e - \phi^s) - \Delta\phi_{eq} = \Delta\phi - \Delta\phi_{eq} = -\Delta\mu/F \tag{4}$$

where consistent with Bazant[55] and Chen et al.,[56] we define $\eta = (\mu_{Li} - (\mu_{Li^+} + \mu_{e^-})/F$. Here, ϕ^e and ϕ^s represent the electrostatic potential in the electrode and the electrolyte respectively, while $\Delta\phi_{eq}$ represents the electrode-electrolyte potential difference at equilibrium. Consistent with conventional electrochemistry notation, the overpotential η thus represents the electric potential above (or below) an equilibrium value required to drive the chemical reaction. This definition of η, along with the specialization $\alpha = 0.5$, which is typical of elementary single-electron transfer reactions, allows us to write Eq. 2 as

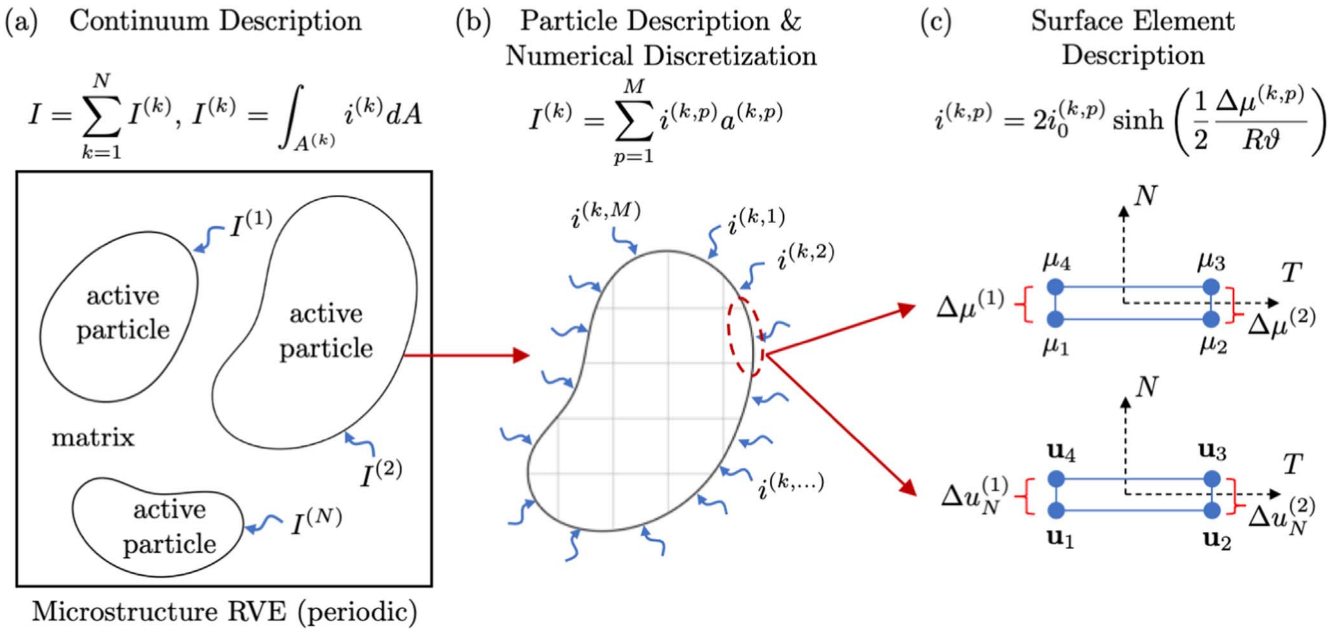

Figure 1. Schematic description of the theoretical and numerical framework employed with a focus on electrochemistry. (a) Continuum description of the microstructure RVE with N particles and galvanostatic conditions enforced. (b) Particle description showing discretization of current over M elements over each particle surface. (c) Description of the surface element in which non-linear reaction kinetics relate local chemical potential jumps at each node pair to the current density at each element.

$$i = 2i_0(\bar{c})\sinh\left(\frac{1}{2}\frac{\Delta\mu}{R\vartheta}\right), \quad [5]$$

which yields a relationship for the local current density at a point on the particle's surface as a function of the chemical potential jump at the same location. Finally, for the microstructure RVE as shown schematically in Fig. 1a, we prescribe periodic boundary conditions.

Particle description and numerical discretization.—Consider now a single particle discretized with finite elements as shown schematically in Fig. 1b. The behavior of this particle can be described through its interfacial and bulk behavior. For clarity, we discuss these behaviors separately.

Interfacial particle behavior.—The particle is discretized with finite elements resulting in M elements on the surface of the particle. Galvanostatic conditions are now enforced by writing the constraint Eq. 1 in the discretized form

$$I = \sum_{k=1}^{N} I^{(k)} \quad \text{with} \quad I^{(k)} = \sum_{p=1}^{M} i^{(k,p)} a^{(k,p)}, \quad [6]$$

where $I^{(k)}$ is the total current over the k-th particle. $i^{(k,p)}$ and $a^{(k,p)}$ are the current density and area of the p-th surface element of the k-th particle. It is important to recall that we allow for and expect current density variations throughout the surface of the particles. Hence, we make no assumptions about current density at any point of the particle surfaces, rather we only enforce the galvanostatic constraint that the total current I be a constant.

To enforce the galvanostatic constraint—and motivated by the physical nature of the problem containing non-linear reaction kinetics at the particle/matrix interface—we introduce surface elements to discretize this interface as schematically shown in Fig. 1c. These elements (analogous to traditional cohesive elements in fracture mechanics) are zero-thickness elements which can be thought of as lines in two-dimensional simulations or surfaces in three-dimensional simulations. Note that the nodes (and hence degrees of freedom) of the bulk continuum elements used to discretize the particle and the nodes on one side of the surface elements are shared.

We enforce the constraint that voltage across all particles be a constant by constraining the chemical potential degrees of freedom on the surface element *adjacent to the matrix* to be equal to $\bar{\mu} = -\bar{V}F$, with $\bar{V} \overset{\text{def}}{=} (V - V_0)$,$V$ the electrode voltage, andV_0 a reference voltage. That is in Fig. 1c, if we envision that μ_1 and μ_2 are connected to the active particles and μ_3 and μ_4 are connected to the matrix, we restrict our surface elements such that $\mu_3 = \mu_4 = \bar{\mu} = -\bar{V}F$ (cf. Di Leo et al.[39]). Numerically, during the finite element solution procedure, we thus have a global constraint that the total current be a constant with the quantity $\bar{\mu}$ an *unknown* degree of freedom which is solved for as part of the global Newton-Raphson finite element solution procedure. The total current I is prescribed only at a single surface element and is distributed (according to the local reaction kinetics) to all other surface elements since they are constrained to have the same chemical potential on the surface side in contact with the electrolyte.

We may now write the reaction kinetics 5 for the current density $i^{(q)}$ at an element on the surface in a discretized form

$$i^{(k,p)} = 2i_0^{(k,p)}\sinh\left(\frac{1}{2}\frac{\Delta\mu^{(k,p)}}{R\vartheta}\right). \quad [7]$$

with $\Delta\mu^{(k,p)}$ the chemical potential jump for the p-th surface element on the k-th particle. Note that the concentration-dependent exchange current density, $i_0^{(k,p)}(\bar{c})$ is computed at each surface element in order to account for variations in concentration along the particle surface. The chemical potential jump $\Delta\mu^{(k,p)}$ is computed using numerical interpolation between the chemical potential jumps $\Delta\mu^{(1)} = \mu_4 - \mu_1$ and $\Delta\mu^{(2)} = \mu_3 - \mu_2$, details of which can be found in Section A of the Supporting Information.

The mechanical behavior of surface elements is also critical as it allows us to capture the manner in which these interfaces can delaminate and damage due to mechanical stresses. The mechanical behavior relates displacement jumps $\Delta\mathbf{u}$, across the interface to the associated tractions $\mathbf{t}$—in a fashion analogous to how chemical potential jump $\Delta\mu$ relates to the current density i across the interface. Broadly, we allow for a finite (yet large) stiffness of the interface, which relates the separation of the surface element nodes to the tractions (stresses) generated at that interface. Damage initiation and evolution criteria are then prescribed to capture interface delamination.

Restricting ourselves to a two-dimensional formulation, the normal t_N, and tangential t_T, tractions at the interface prior to damage initiation are computed through

$$t_N = K_N\Delta u_N, \quad \text{and} \quad t_T = K_T\Delta u_T, \quad [8]$$

with Δu_N and Δu_T denoting the normal and tangential displacement jumps respectively. Note that in Fig. 1c, for brevity, we have only schematically depicted the normal displacement jump. Following Camanho and Da Vila,[57] damage initiation is taken to occur through a quadratic failure criteria of the form

$$\left(\frac{\langle t_N\rangle}{t_N^{\text{cr}}}\right)^2 + \left(\frac{t_T}{t_T^{\text{cr}}}\right)^2 = 1, \quad [9]$$

where t_N^{cr} and t_T^{cr} are the normal and tangential cohesive strengths (i.e. the peak value these tractions may attain when the deformation is purely normal or purely tangential to the interface), and $\langle\cdot\rangle$ denotes the Macaulay bracket.

Mechanical damage evolution is modeled through the introduction of a scalar variable, D_{mech}, which represents the overall state of mechanical damage for a surface element. During damage evolution, tractions decay linearly with mechanical damage and are computed through

$$\begin{aligned} t_N &= \begin{cases} (1 - D_{\text{mech}})K_N\Delta u_N, & \text{if} \quad K_N\Delta u_N \geqslant 0, \\ K_N\Delta u_N, & \text{otherwise (to avoid surface inter} \end{cases} \\ t_T &= (1 - D_{\text{mech}})K_T\Delta u_T. \end{aligned} \quad [10]$$

To model the evolution of damage it is common to introduce an effective displacement jump $\delta_m = (\langle\Delta u_N\rangle^2 + \Delta u_T^2)^{1/2}$. We may then model linear softening of tractions due to mechanical damage through an evolution equation for D_{mech} of the form

$$D_{\text{mech}} = \frac{\delta_m^f(\delta_m^{\max} - \delta_m^0)}{\delta_m^{\max}(\delta_m^f - \delta_m^0)}, \quad D_{\text{mech}} \in [0, 1]. \quad [11]$$

Here, δ_m^0 is the effective displacement jump at damage initiation, δ_m^f is the effective displacement jump at complete failure, and $\delta_m^{\max}$ is the maximum value of the effective displacement attained during the loading history, a monotonically increasing quantity.

Considering positive normal displacement jumps, the effective displacement jump at damage initiation, δ_m^0 may be written as

$$\begin{aligned} \delta_m^0 = \delta_N^0\delta_T^0\sqrt{\frac{1+\beta^2}{(\delta_T^0)^2 + (\beta\delta_N^0)^2}} &= \frac{t_N^{\text{cr}}}{K_N}\frac{t_T^{\text{cr}}}{K_T} \\ &\times \sqrt{(1+\beta^2)\left(\left(\frac{t_T^{\text{cr}}}{K_T}\right)^2 + \beta^2\left(\frac{t_N^{\text{cr}}}{K_N}\right)^2\right)^{-1}}. \end{aligned} \quad [12]$$

In writing 12 we have made use of the fact that $\delta_N^0 = t_N^{\mathrm{cr}}/K_N$ and $\delta_T^0 = t_T^{\mathrm{cr}}/K_T$. In Equation 12, $\beta = \Delta u_T/\Delta u_N$ is the mode-mixity parameter. Similarly, the effective displacement jump at complete failure, δ_m^f may be written as

$$\delta_m^f = \frac{2(1+\beta^2)}{K\delta_m^0}\left[\left(\frac{1}{G_N}\right) + \left(\frac{\beta^2}{G_T}\right)\right]^{-1} \qquad [13]$$

with G_N and G_T the normal and tangential *fracture energies*. In writing Equation 13 we have further specialized our model such that $K = K_N = K_T$.

As shown from Eqs. 12 and 13, the material properties for this model are the stiffnesses, presumed to obey $K = K_N = K_T$, the fracture energies $\{G_N, G_T\}$, and the critical tractions for damage initiation $\{t_N^{\mathrm{cr}}, t_T^{\mathrm{cr}}\}$. Of these parameters, K may be prescribed arbitrarily provided that it is large enough not to introduce unwanted compliance in the simulation. The physical material parameters are thus only the normal and tangential critical tractions $\{t_N^{\mathrm{cr}}, t_T^{\mathrm{cr}}\}$ and the fracture energies $\{G_T, G_N\}$. Note that the mode-mixity parameter $\beta = \Delta u_T/\Delta u_N$ depends on the loading path and is not a material property. The limiting case $\beta \to 0$ corresponds to pure normal separation, while the limiting case $\beta \to \infty$ corresponds to pure shear.

For numerical purposes, we employ a viscous regularization scheme to model the evolution of mechanical damage at the interface. Following Hamitouche et al.,[58] we introduce a small viscosity λ (small with respect to the characteristic time increment) and compute the viscous mechanical damage according to

$$D_{\mathrm{mech}}^v = D_{\mathrm{mech}} - \lambda\frac{\dot{\delta}_m}{\delta_m}. \qquad [14]$$

Henceforth, when referring to mechanical damage we are employing the viscous damage defined above. Viscosity values employed in all simulations in this work ranged between 0.1 and 0.3 s.

Finally, to model the effect of mechanical damage on transport kinetics, the current density across the interface, viz. 7, is penalized through

$$i^{(k,p)} = (1 - D_{\mathrm{chem}})2i_0^{(k,p)}\sinh\left(\frac{1}{2}\frac{\Delta\mu^{(k,p)}}{R\vartheta}\right), \quad \text{with}$$
$$D_{\mathrm{chem}} \in [0, 1], \qquad [15]$$

where D_{chem} denotes the chemical damage. We specialize the relationship between D_{mech} and D_{chem} in when we specialize our models to a particular physical system. As captured through Equation 15, this model will allow one to capture the loss of chemical reactivity at a point on the surface of an active particle due to concurrent mechanical damage. The effect of this will be studied in detail in the simulation results shown in this work.

Bulk particle behavior.—We present here, for completeness, a brief summary of the coupled, chemo-mechanical, diffusion-deformation theory for modeling the bulk behavior of active particles. Details of the theoretical framework may be found in Di Leo et al.[39] This framework models coupling of species diffusion with large elastic-plastic deformations due to volumetric changes caused by the diffusing species. The active particle is treated as a homogenous mixture of the active material and Li, with the molar concentration of Li per unit reference volume denoted by c_{R} and per unit current volume by $c = J^{-1}c_{\mathrm{R}}$, with $J = \det\mathbf{F}$, and $\mathbf{F}$ the deformation gradient. We further define a normalized concentration $\bar{c} = c_{\mathrm{R}}/c_{\mathrm{R,max}} \in [0, 1]$. We employ the decomposition $\mathbf{F} = \mathbf{F}^e\mathbf{F}^p\mathbf{F}^s$ of the deformation gradient into elastic, plastic and swelling parts, where

$$\mathbf{F}^s = (J^s)^{1/3}\mathbf{1}, \quad \text{with} \quad J^s = 1 + \Omega(c_{\mathrm{R}} - c_{\mathrm{R0}}), \qquad [16]$$

is the swelling distortion, Ω is a constant partial molar volume of the intercalating Li in the body, and c_{R0} is the initial concentration of Li. Further, we assume $J^p = \det\mathbf{F}^p = 1$ such that plastic deformation be volume conserving. The Cauchy stress is given by

$$\mathbf{T} = J^{e-1}\left(2G(\bar{c})\mathbf{E}_{\mathrm{H}}^e + \left(K(\bar{c}) - \frac{2}{3}G(\bar{c})\right)(\mathrm{tr}\,\mathbf{E}_{\mathrm{H}}^e)\mathbf{1}\right), \qquad [17]$$

where $G(\bar{c})$ and $K(\bar{c})$ are concentration-dependent Shear and Bulk moduli respectively, and $\mathbf{E}_{\mathrm{H}}^e$ is the spatial logarithmic elastic strain. To complete the mechanical portion of the theory, plastic distortion is taken to evolve according to

$$\dot{\mathbf{F}}^p = \mathbf{D}^p\mathbf{F}^p, \qquad \text{with} \qquad \mathbf{D}^p = \dot{\bar{\epsilon}}^p\left(\frac{3\mathbf{M}_0^e}{2\bar{\sigma}}\right),$$
$$\dot{\bar{\epsilon}}^p \geqslant 0, \qquad \mathbf{F}^p(\mathbf{X}, 0) = \mathbf{1}, \qquad [18]$$

where $\bar{\sigma} \overset{\mathrm{def}}{=} \sqrt{3/2}\,|\mathbf{M}_0^e|$ defines an equivalent tensile stress and $\dot{\bar{\epsilon}}^p$ denotes an equivalent tensile plastic strain rate. The specific form of the plastic flow rule will be specified in the numerical examples described in subsequent sections corresponding to the physical problem under consideration.

Turning attention to diffusion, spatial flux $\mathbf{j}$, of the intercalating Li is taken to depend on the spatial gradient grad μ, of the chemical potential through

$$\mathbf{j} = -m\,\mathrm{grad}\,\mu, \quad \text{with} \quad m = \frac{D_0}{R\vartheta}c(1 - \bar{c}) \geqslant 0 \quad \text{the mobility.} \qquad [19]$$

Here, D_0 is a constant diffusion coefficient. The chemical potential of Li in the active particle is given by,

$$\mu = \mu^0 + R\vartheta\ln\left(\gamma\frac{\bar{c}}{1 - \bar{c}}\right) - \Omega\frac{1}{3}\mathrm{tr}\,\mathbf{M}^e, \qquad [20]$$

where we have have defined an activity coefficient γ through $R\vartheta\ln(\gamma) = \sum_{n=2}^{7} a_n \cdot n \cdot \bar{c}^{(n-1)}$, whose coefficients a_n are fitted to experimental open circuit potential data. Importantly, the chemical potential, Equation 20 , is *stress-coupled* through the Mandel stress $\mathbf{M}^e$ which may be related to the traditional Cauchy stress $\mathbf{T}$ through an elastic rotation and elastic volumetric scaling.

The above fields are governed by two partial differential equations expressed in the deformed body. As is standard, the mechanical problem (displacement field) is governed by a local force balance, div $\mathbf{T} = 0$, with appropriate boundary conditions requiring that displacement or traction be prescribed at a given point on the exterior of the body. The lithium diffusion problem (chemical potential field) is governed by mass balance, $\dot{c}_{\mathrm{R}} = -J\,\mathrm{div}\,\mathbf{j}$, where appropriate boundary conditions are that one may either prescribe the chemical potential or the spatial flux at a given point on the surface of the body. Finally, we note that current density i as described in the previous section and normal flux of species $j = \mathbf{j}\cdot\mathbf{n}$, with $\mathbf{n}$ the normal to the surface of an active particle at a point, are related simply through $j = -i/F$. Details of the numerical implementation, with a focus on the implementation of the chemo-mechanical surface elements, is presented in Section A of the Supporting Information following the work of Di Leo[59] and Chester et al.[60]

Next, we apply our framework to model the behavior of different multi-particle electrode configurations. We begin in the next section with a simple demonstration of a two-particle system to illustrate the capabilities of the framework in modeling galvanostatic conditions and capturing current distributions across particle surfaces. In the subsequent sections we consider a multi-particle electrode composed of hollow, double-walled a-Si active particles, which are chemically connected, but mechanically isolated, representative of the limiting case in a liquid LIB where mechanical stress transfer through the matrix is negligible. Finally, we model a solid-state composite cathode microstructure where mechanical load transfer through the SSE is significant.

Numerical Framework Demonstration

To illustrate our numerical framework, we present here a simple simulation of a two particle system. Both particles are embedded in an elastic matrix and their surfaces are discretized with the chemo-mechanical surface elements detailed in the section above. As described by Equation 15, we allow here for mechanical degradation of the interface due to normal stresses leading to a loss in local reactivity. The particles are modeled as chemo-elastic (no plastic deformation) and incur 2% volume decrease when fully lithiated. The specific material parameters are the same as those used in the section on modeling interfactial damge of SSBs. For this illustration, we impose galvanostatic charging conditions at a C-Rate of 1C with the additional aforementioned constraint that voltage over the particle surfaces be a constant. Mechanically, we impose periodic boundary conditions on the electrode domain, effectively treating it as a representative volume element (RVE). For illustration purposes, we induce significant variations in current distribution between particles by assigning the left particle a reaction constant $k_0 = 9 \cdot 10^{-6}$ mol/(m^2 s), while the right particle has a reaction constant $k_0 = 9 \cdot 10^{-7}$ mol/(m^2 s).

Figure 2a shows the total current flowing to the left (blue line) and right particle (orange line) as well as into the entire simulation domain (yellow line) as a function of time. We observe that we can successfully maintain galvanostatic charging conditions while current distribution to the two particle varies in time. Until time $t = t_a$, no interfacial damage occurs and the total current is distributed with more current flowing to the left particle owing to its faster reaction kinetics.

After $t = t_a$, interfacial damage occurs over both particles with mechanical decohesion starting in the left particle first owing to its higher extent of lithiation (and hence higher mechanical stresses at the interface). Mechanical degradation now causes current to redistribute over both particles, as dictated by the interplay of two mechanisms: i) the variation in reaction constants among particles, and ii) the state of mechanical damage on the particle surface. As interfacial damage across both particles evolves while $t_a < t < t_b$, the interplay of these mechanisms first leads to an increase in current flowing to the left particle, while current flowing to the right particle decreases to maintain the galvanostatic charging condition.

Figure 2b shows the current density over each particle as a function of the normalized contour distance (i.e perimeter) of the particle at time $t = t_b$, the start of the normalized contour variables is noted in Fig. 2d as s_1 and s_2. We can clearly observe the inherent coupling between mechanical degradation and interface kinetics (i.e current density). Here, we observe regions over the particles with zero (or near zero) current density as they have become heavily or completely decohered. These regions, marked by white arrows in Fig. 2d, represent elements at the surface of both particles which have completely decohered and are now chemically isolated and unable to carry current. In Fig. 2d we show contours of normalized concentration, $\bar{c}$, over the particle simulation domains and contours

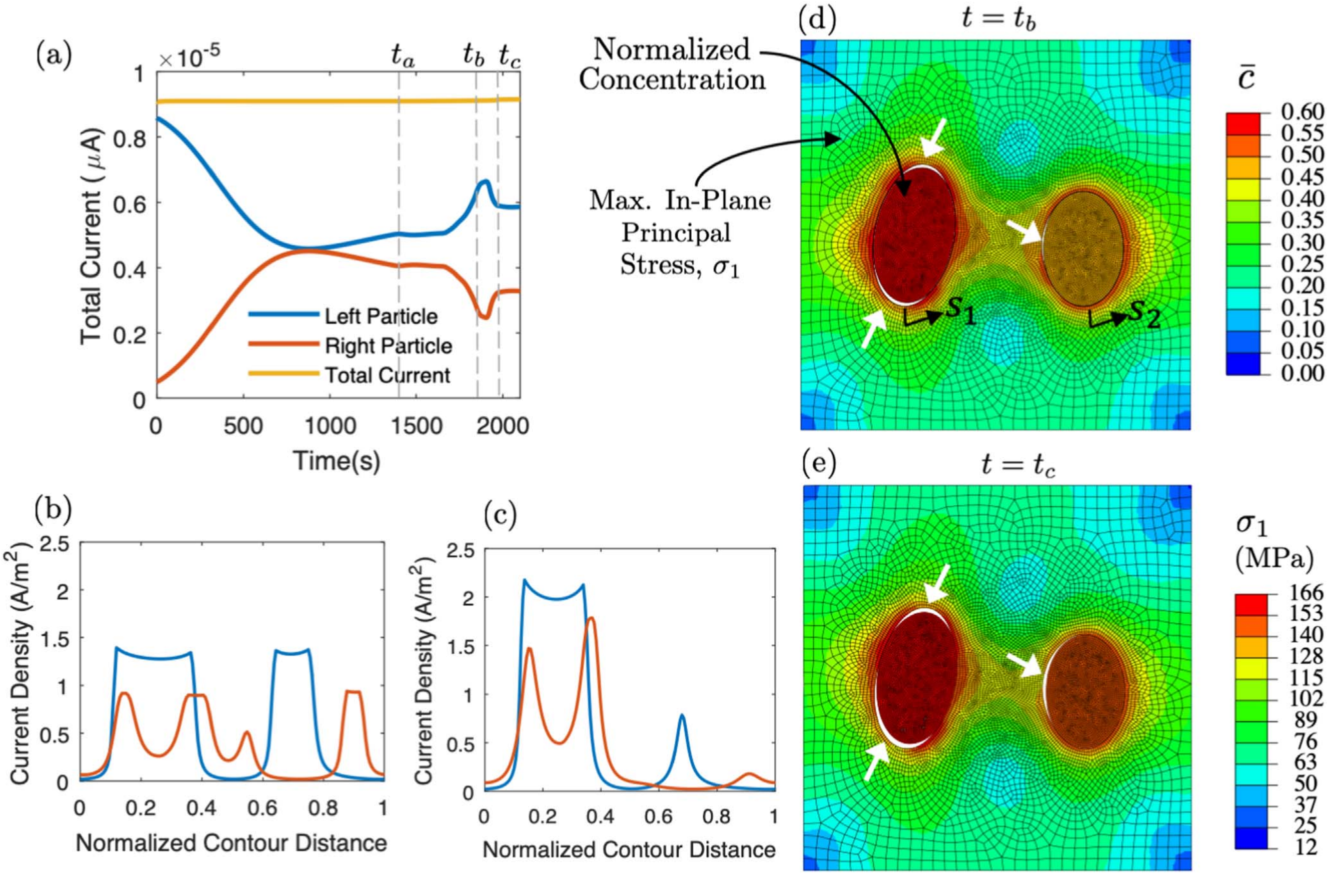

Figure 2. Example of a two-particle numerical simulation. (a) Total current distribution to both particles as well as the entire simulation domain, illustrating the ability to capture galvanostatic charging conditions. (b)–(c) Local current densities as a function of the normalized distance (s_1, s_2) along the particle surface taken at time $t = t_b$ and $t = t_c$. (d)–(e) Contours of maximum in-plane principal stress, σ_1 over the matrix and normalized concentration, $\bar{c}$ over the particle domain taken at time time $t = t_b$ and $t = t_c$. Also illustrated in white are regions of decohered interface.

of the maximum in-plane principal stress, σ_1 over the matrix at time $t = t_b$.

After time $t = t_b$, a significant portion of the surface of the left particle is decohered and it can no longer sustain sufficiently large currents, thus there is a decrease in current to the left particle as shown in Fig. 2a. In turn, to preserve a state of galvanostatic charging, the right particle sees an increase in total current. Figure 2c shows the current density over each particle as a function of the normalized contour distance at time $t = t_c$. We can observe across both particles that most of the surface is no longer carrying any significant current and the portion which remains intact carries a higher current density when compared to Fig. 2b. Figure 2e shows the corresponding simulation results at $t = t_c$ where we can observe significant damage accumulated now over both particles.

This simple numerical example serves to illustrate the ability of our numerical framework—enabled by the development of chemo-mechanical surface elements—to: i) capture the chemo-mechanical interactions between particles under galvanostatic charging and the associated non-uniform distribution of current to different particles, and ii) capture the non-uniform local current densities which develop across each particle. In the sections to follow we deploy this numerical framework to study composite electrode systems of relevance to both liquid LIBs and SSBs.

Multi-particle Interactions in Double Walled a-Si Nanotube Electrodes

We consider now a multi-particle electrode composed of hollow double-walled a-Si active particles which are chemically connected, but mechanically isolated, representative of the limiting case in a liquid LIB in which mechanical stress transfer through the electrolyte is negligible. The simulation mimics the experimental research of Wu et al.,[45] who manufactured a new anode architecture composed of an ensemble of double-walled aSi nanotubes with the particular objective of preventing failure of the solid electrolyte interphase (SEI), see Fig. 3a. As has been studied in the literature, volumetric expansions of active particles can induce large mechanical stresses on the SEI layer, causing it to fracture and fail.[61–63] The double-walled aSi nanotubes proposed by Wu et al.[45] consist of an aSi hollow nanotube, whose exterior is oxidized to form a mechanically stiff SiO_2 layer, thus forming a double-walled structure. Due to the high relative mechanical stiffness of the exterior SiO_2 layer when compared to the softer aSi core, volumetric expansions are accommodated primarily through expansion into the hollow internal cavity and minimal strains and stresses are incurred by the SEI layer forming on the exterior surface. In our previous research efforts,[39] we investigated the chemo-mechanical behavior of a single hollow double-walled nanotube to gain insight on the coupling between mechanics and chemistry in such a confined geometry. However, we did not address the multi-particle nature of the electrode or the potential for mechanical damage.

In this work, each individual tube is modeled through an axisymmetric row of finite elements as shown in Figs. 3b and 3c. Here, we assume the length of the nanotubes to be much larger than their diameter. This effectively enables one to model each nanotube as a row of elements with the flux of Li ions occurring in the radial direction only. The bottom surface of each row of elements is constrained to have zero displacement in the $\mathbf{e}_z$ direction, while the top surface is constrained to remain flat, but may displace. The simulation domain is broken into two parts, namely an aSi core and the confining SiO_2 shell, with chemo-mechanical surface elements discretizing the interface between the two domains, see Fig. 3c. The SiO_2 shell is prescribed a purely elastic mechanical behavior and we neglect transport of Li through this layer. The aSi obeys the chemo-mechanical framework described in the section above. Following Di Leo et al.,[39] the plastic behavior of the aSi shell is modeled by introducing a positive-valued, stress-dimensioned, and concentration-dependent yield strength $Y(\bar{c}) > 0$, and assuming a no-flow condition of the form $\bar{\sigma} \leqslant Y(\bar{c})$. During plastic flow, $\dot{\bar{\epsilon}}^p > 0$, and the equivalent tensile stress is taken to be equal to a rate-dependent flow strength,

$$\bar{\sigma} = Y(\bar{c}) + Y_* \left(\frac{\dot{\bar{\epsilon}}^p}{\dot{\epsilon}_0} \right)^{1/m}, \quad \text{with}$$

$$Y(\bar{c}) = Y_{\text{sat}} + (Y_0 - Y_{\text{sat}}) \exp\left(-\frac{\bar{c}}{\bar{c}_*} \right), \tag{21}$$

where $Y_* > 0$ is a positive-valued, stress-dimensioned constant, $\dot{\epsilon}_0$ is a reference tensile plastic strain rate, and m is a measure of the strain-rate sensitivity of the material. All material properties for the aSi and SiO_2 are adopted from the work of Di Leo et al.[39] and the reader is referred to this reference for numerical values.

The multi-particle behavior is modeled by including N simulation domains representing N particles as shown in Fig. 3c. It is important to note that although these particles are mechanically isolated (in the sense that they do not contact each other), they are *chemically*

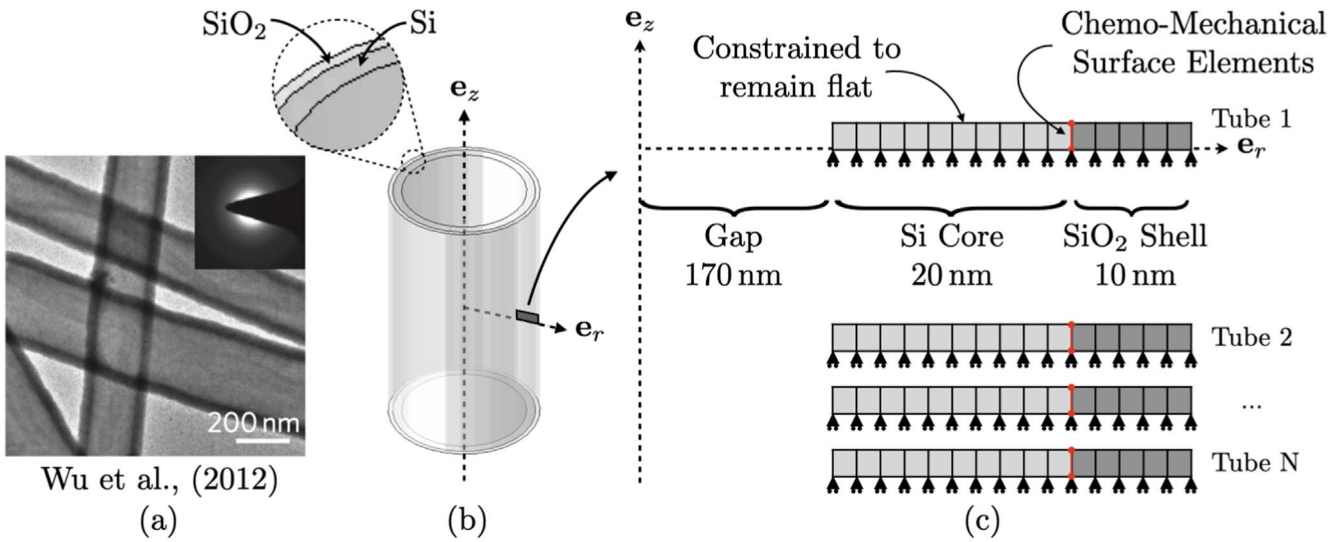

Figure 3. Multi-particle modeling of hollow double-walled nanotubes. (a) Shows a representative SEM image from the experiment of Wu et al. Reprinted with permission from Ref. 45. (b) Shows a schematic three-dimensional representation of a single tube denoting the simulation domain as a single sliver of the tube in the axial direction. (c) Shows the numerical discretization using finite elements of the aSi core and the SiO_2 shell, including the discretization of the interface using chemo-mechanical surface elements.

connected through the presence of the chemo-mechanical surface elements. Through these elements, we enforce galvanostatic charging conditions across all particles under the assumption of a constant Voltage maintained across the active particle-electrolyte interface.

The numerical framework described above allows us to investigate the interplay of mechanics and chemistry in multi-particle systems and the associated effect on electrochemical performance. First, we investigate the effect of statistical variations in electrochemical properties—namely the reaction constant k_0 between the active particles and the electrolyte—on current distribution across particles and interfacial mechanical stress build up. Second, we investigate the potential presence and role of interfacial damage on electrochemical performance and capacity fade while cycling. In all of the following studies, we consider $N = 50$ active particles.

Electrochemical performance and stress generation with varying reaction constant $\mathbf{k_0}$**.—**We consider first the effects that would arise in a multi-particle system from having a distribution of reaction constants k_0 affecting the reaction kinetics at the interface of the particles and the electrolyte. Such a variation in k_0 may arise experimentally due to a number of mechanisms including poor bonding of the aSi/SiO_2 interface, failure of the SEI, and pre-existing damage of the active material during manufacturing. The reaction constant k_0 dictates reaction kinetics at the interface (cf. Eq. 3), which is modeled through the chemo-mechanical surface elements, and is prescribed a log-normal distribution. The mean of the distribution is prescribed as the logarithm of the baseline reaction constant $k_0 = 3.25 \cdot 10^{-7}$ mol/(m^2 s) reported in Di Leo et al.[39] The standard deviation (SD) is varied in our investigation and we consider values of SD = 1.0 and SD = 2.0. This choice is motivated to produce significant variations in local current distribution occurring over the simulation domain in order to understand how these local variations affect the overall electrochemical response of the multi-particle system and the concurrent stress generation. Consistent with the experiments of Wu et al.,[45] the simulation domain is cycled under galvanostatic conditions at a C-Rate of 1C with voltage limits of 0.01 V and 1 V for three half-cycles. For conciseness, we do not show snapshots of the evolution of the simulation domain in the main manuscript. However, an animation of the simulation is included in the supplementary movie S1_aSi_Cycling.mp4 is available online at stacks.iop.org/JES/168/030515/mmedia. We note that in this first set of simulation results *we do not allow for mechanical interfacial damage*, which will be considered in subsequent sections.

To understand the effect on electrochemical performance of variations in k_0, we compute both the local (single nanotube) and global (whole ensemble of nanotubes) voltage vs state-of-charge (SOC) response during cycling. Recall that Voltage is assumed to be constant throughout the simulation domain and is an unknown which is solved for in the finite element framework in order to ensure the galvanostatic charging constraint is met. In generating the Voltage vs SOC curves subsequently shown, we ignore the results from the first half-cycle in our simulations.

The simulation results are shown in Fig. 4. First, we focus on the individual behavior of three of the 50 nanotube particles from the SD = 1.0 simulation, which have been chosen to represent the lowest, average, and highest reaction constants present in the simulation and differ in k_0 value by approximately one order of magnitude. An important feature of multi-particle simulations evident in Fig. 4a is the "smoothing" of the Voltage vs SOC behavior of the individual particles as cycling is reversed. This feature is enhanced as the reaction constant k_0 is decreased, as shown in Fig. 4a.

This behavior is tied to chemical interactions between particles with varying k_0, which in turn impacts local current distribution to individual particles as shown in Fig. 4b, where we compare the current applied to the entire simulation domain (purple line, right y-axis) with the local current experienced by the three nanotube particles under investigation (left y-axis). While the entire simulation domain experiences a sharp change in total current during cycle reversals (purple line), the individual particles experience a gradual variation in current, which depends on their local reaction kinetics. Particles with sluggish (low) reaction kinetics experience a gradual reversal in current, which in turn affects the contribution of the overpotential to the total Voltage vs SOC behavior and results in "smoothening" of the Voltage vs SOC behavior as shown in Fig. 4a.

The global behavior of the system is shown in Fig. 4c. Results are shown for two simulations with log-normal k_0 distributions with a standard deviation of SD = 1.0 and SD = 2.0 as well as for a single-particle (standard deviation of zero). Also shown is the experimentally measured response of Wu et al.[45] The "smooth" transition in voltage during cycle reversals can be observed in the experimental results shown and is also captured when a significant variation in k_0 is included in the multi-particle simulations developed in this work. As shown in Fig. 4c, this feature cannot be captured when modeling a single particle system as the jump in current during cycle reversal will always lead to a jump in voltage. This illustrates one of the benefits of developing simulation tools which accurately model galvanostatic charging conditions in multi-particle electrode systems. Further, variation in local current distribution (see Fig. 4b) also has a significant impact on the generation of stresses and potential for initiation and evolution of mechanical damage as investigated next.

To investigate the interplay between chemical performance and mechanics, we focus on the generation of normal stresses at the aSi/SiO_2 interface. Here, we demonstrate the manner in which variations in local reaction kinetics of each particle—as prescribed through a variation in the reaction constant k_0—affect the generation of mechanical stresses at these interfaces. Figure 5a shows the normal (i.e. radial direction in Fig. 3) component of stress $\sigma_{rr} = \tau_N$ at the aSi/SiO_2 interface as a function of the local state-of-charge of each particle for the same three particles discussed before. As can be observed, the interfaces develop different levels of normal stress, which are largely correlated to the local state-of-charge of each particle. The local SOC of each particle in turn differs due to variations in reaction constant, which promote a non-uniform state of lithiation across particles during cycling.

This behavior is a direct outcome of the elastic-plastic constitutive behavior used to model the a-Si core and the large deformation kinematics, which result in an increase (either negative or positive) of normal interfacial stresses as the a-Si core becomes further lithiated. Importantly, differences between these curves *at a given state-of-charge* arise from the *mechanical strain-rate sensitivity* of the material. Since particles experience different currents, they also experience different loading rates, which in turn changes their mechanical response. In summary, the magnitude of normal interfacial stresses is controlled both by the total amount of Lithium reacted into the a-Si core and the rate of lithiation.

From an interfacial mechanical damage perspective (which will be further investigated in the next section), this poses an interesting question, which is to investigate the C-Rate sensitivity of interfacial mechanical stresses. Figure 5b shows the normal interfacial stresses as a function of the local SOC for the nanotube with a reaction constant $k_0 = 3.25 \cdot 10^{-7}$ mol/(m^2 s). Three simulations are shown with C-Rates of 1C, 1/10C, and 1/20C. We can observe the *counter-intuitive result* that a decrease in C-Rate does not necessarily lead to a decrease in the maximum (positive or negative) normal interfacial stresses experienced at the aSi/SiO_2 interface. The rather constant nature of the maximum normal interfacial stresses during cycling shown in Fig. 5b is due to both the extent of lithiation and the mechanical strain-rate sensitivity of the material. At higher C-Rates, we achieve a lower local SOC for each particle, which would in turn yield lower interfacial stresses. However, mechanical strain-rate sensitivity is amplified at higher C-Rates, which in turn increases interfacial stresses. These two competing mechanisms for the particular case of an a-Si/SiO_2 double-walled nanotube counteract

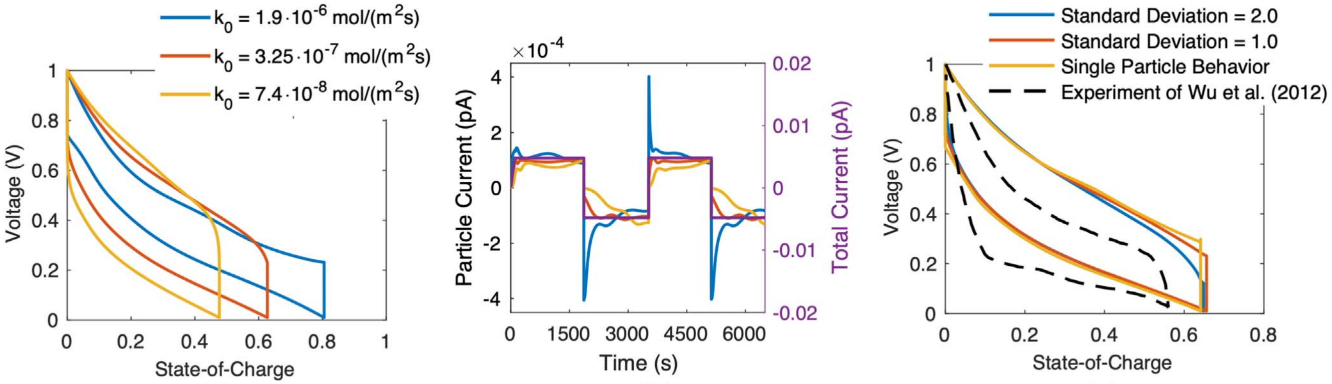

(a) (b) (c)

Figure 4. Simulation results for a 50-particle system with a statistical distribution in reaction constant k_0. (a) Local (individual nanotube) voltage vs state-of-charge behavior for three particles spanning the range of k_0 values considered. (b) Current vs time response for the three particles under consideration compared against the total current in the simulation domain. (a) and (b) are for the case of SD = 1.0. (c) Global (entire simulation domain) voltage vs state-of-charge behavior for a single particle, simulations with k_0 distributions with SD = 1.0 and SD = 2.0, and the experimentally measured response of Wu et al.[45]

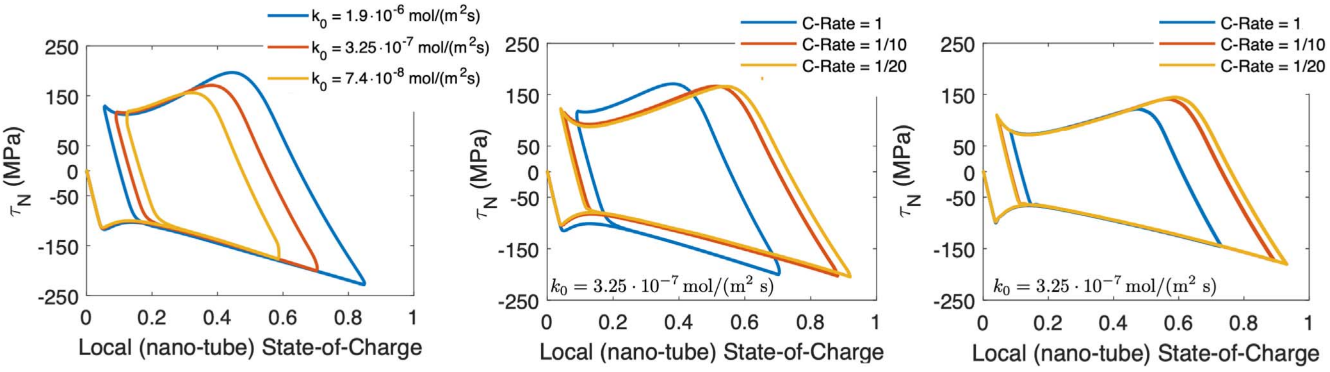

(a) (b) (c)

Figure 5. Interfacial normal stress, τ_N at the aSi/SiO$_2$ interface as a function of local (nanotube) SOC. (a) Results for three representative particles spanning the range of k_0 values considered at a C-Rate of 1C. (b)–(c) Results for a particle with a reaction constant of $k_0 = 3.25 \cdot 10^{-7}$ mol/(m^2 s) at three different C-Rates, with (b) mechanical strain-rate sensitivity taken into consideration, and (c) mechanical strain-rate sensitivity neglected.

each other to yield a fairly constant normal interfacial stress with varying C-Rates.

To further illustrate this competition, Fig. 5c shows the same result where the constitutive behavior of the a-Si core has been modified to have *no strain-rate sensitivity* by setting the parameter $Y_* = 0$ in 21. As shown in Fig. 5c, normal interfacial stresses are now entirely governed by the local state-of-charge of the particular particle and we can observe that lower C-Rates always lead to higher interfacial stresses.

It is important to note that this behavior—which is counter-intuitive to the usual experience that higher C-Rates are always mechanically detrimental—arises from the fact that here we focus on the interfacial mechanical stresses at the aSi/SiO$_2$ interface rather then the bulk stresses developed in either the core or the shell. Bulk stresses generally arise due to large gradients in concentration or volumetric expansion under mechanical constraint. However, owing to the nano-metered sized geometry of this particular anode design, concentration gradients are negligible and bulk stresses in this particular geometry arise from the mechanical constraint imposed by the SiO$_2$ shell on the aSi core, which is no longer free to expand. An in-depth discussion on the single particle mechanics of this anode geometry can be found in Di Leo et al.[39]

The results shown in this section illustrate the complex nature of multi-particle behavior when taking into consideration potential variations in local reaction kinetics by varying the reaction constant k_0 through a statistical distribution. The results demonstrate that variation in k_0 can significantly affect local current distribution among the various active particles and in turn influence the global voltage vs SOC behavior. Further, variation in k_0 can also significantly affect the generation of mechanical stresses with a focus on the development of normal interfacial stresses at the aSi/SiO$_2$ interface. These stresses could potentially lead to mechanical damage through decohesion of the interface, which would in turn affect chemical connectivity of the particles to the electrode. In the following section, we investigate capacity loss in this prototypical liquid LIB electrode due to mechanical damage and loss of connectivity through use of the developed surface elements.

Capacity loss due to mechanical interfacial decohesion.—We now shift our attention to modeling capacity loss due to mechanical interfacial decohesion in the electrode under consideration. Unlike the previous section, we consider now a statistical variation in mechanical properties associated with the cohesive strength of the aSi/SiO$_2$ interface, while maintaining the reaction rate constant at $k_0 = 3.25 \cdot 10^{-7}$ mol/(m^2 s). The choice of varying the cohesive strength t_N^{cr}, as opposed to the reaction rate k_0, in this section is made for pragmatic reasons. The material property, k_0 has been previously experimentally determined in Ref. 39 while the specific value of t_N^{cr}, as will be discussed below, is unclear from the literature and can vary over a significant range depending on manufacturing conditions.

Across the simulation domain containing $N = 50$ active particles, we prescribe the normal cohesive strength t_N^{cr} using a normal distribution with a mean strength of 160 MPa and a standard deviation of 70 MPa. The mean cohesive strength is chosen to approximately match with the average normal stresses at the interface across an ensemble of nanotubes with varying k_0 as determined in section 4.1. The standard deviation is such that at least 50% of the particles will incur mechanical damage during cycling at different C-Rates. We consider only normal mechanical damage (i.e. $\beta = 0$ in Eqs. 12 and 13) with t_N^{cr} as defined above and simply take t_T^{cr} in Equation 9 to be a large number to guarantee no damage initiation due to tangential interfacial stresses. The prescribed variation in cohesive strength is intended to showcase the utility of our modeling framework to study the interplay of chemo-mechanical interactions and role of damage on electrochemical performance and capacity fade through consecutive cycling. The normal stiffness of the interface is taken equal to $K_N = 6 \cdot 10^{11}$ MPa/m, which is sufficiently large not to introduce artificial compliance in the simulation domain. To define damage evolution, we use a baseline fracture energy of $G_N = 0.25\ \mathrm{J\ m^{-2}}$. In combination, these material properties define all the necessary parameters for the constitutive behavior summarized in Eqs. 9 to 11. Finally, for simulations in this section, we consider chemical damage to evolve equal to mechanical damage, that is $D_{\mathrm{chem}} = D_{\mathrm{mech}}$. The relationship between mechanical and chemical damage need not be one-to-one and it is possible that small amounts of mechanical damage lead to significant chemical damage and loss of reactivity at a point. Owing to the lack of experimental data on the mechanical/chemical damage of aSi/SiO_2 interfaces, here we simply prescribe the two equal so as to not introduce further modeling parameters in the simulation.

The simulation domain is cycled under galvanostatic conditions with varying C-Rates and voltage limits of 0.01 and 1 Volts. We simulate 27 cycles of the electrode with a baseline C-Rate of 1/2C and alternating cycles at higher and lower rates. The complete sequence of C-Rates is given by

$$\text{C-Rate} \in [1/2\text{C},\ 2\text{C},\ 1/2\text{C},\ 4\text{C},\ 1/2\text{C},\ 1/4\text{C},\ 1/2\text{C},\ 1/10\text{C},\ 1/2\text{C}] \qquad [22]$$

where three cycles are spent at each particular C-Rate. This sequence allows us to asses how damage incurred at higher or lower C-rates—with respect to the baseline 1/2C rate—affects electrochemical performance. By computing the capacity of the electrode at a C-Rate of 1/2C before and after cycling at a different rate, we can understand how damage incurred at a particular rate affects the capacity of the electrode. Following Di Leo et al.,[39] a maximum capacity of 3.579 Ah g^{-1} for Si is used to convert SOC data to an equivalent capacity.

Simulation results are shown in Fig. 6. The top row shows the voltage vs SOC response for the entire simulation domain, while the bottom row shows the simulation domain, where in the aSi domain we show contours of the normalized concentration $\bar{c}$. The SiO_2 shell is shown as a grey region without contours. Figure 6a shows the electrochemical response of the electrode at the end of the third conditioning cycle at a C-Rate of 1/2C at which point the battery accrues a significant amount of damage. We term the first three cycles of the system at the baseline rate as conditioning cycles since during these cycles a significant amount of damage is incurred leading to a new stable baseline voltage vs SOC response different from that expected from the pristine electrode without any damage. If the battery is continuously cycled at the baseline C-Rate of 0.5C following the initial three conditioning cycles, the electrochemical response would remain unchanged. Figure 6c highlights with red arrows the particles which have completely decohered from their SiO_2 shells during the conditioning cycles and are now chemically isolated from all other particles. Due to mechanical decohesion, the electrode stabilizes to a new electrochemical window with a significantly reduced capacity (blue line) compared against a simulation without damage (yellow line). Figure 6b shows the voltage vs SOC response of the aSi anode at the end of the 9th (blue line), 12th (orange line) and 15th (purple) cycle during which the electrode is intermittently charged at a C-Rate of 4C. By comparing the voltage vs SOC behavior during cycling at the baseline 1/2C rate before (blue line) and after (purple line) the intermittent 4C cycles, we can visually see the additional loss in capacity as the electrochemical window shrinks. Figure 6d, highlights with red arrows the additional particles which completely decohere from their SiO_2 shells during the intermittent 4C cycling. The supplementary movie S2-aSi-Damage.mp4 shows a complete animation of this process.

Capacity loss due to interfacial decohesion is best characterized through a graph of capacity as a function of cycle number as shown in Fig. 7. Here, simulation results without (blue line) and with (orange line) damage are displayed. The response of the simulated electrode without mechanical damage (blue line) in Fig. 7 matches the theoretical expectations for galvanostatic charging within a fixed voltage window, where simulations with higher C-Rates have lower capacity and lower C-rates have higher capacity. It is important to note that the baseline capacity at a C-rate of 1/2C remains unchanged in the absence of mechanical damage and loss of electrochemical contact. The simulated electrode response with mechanical damage (orange line) shown in Fig. 7 is markedly different. A large amount, approximately 75%, of the electrode's capacity is lost in the first three conditioning cycles. This correlates with a large number of active particles becoming decohered from their SiO_2 shells as shown in Fig. 6c. During subsequent cycling at 2C, we do not incur additional damage as we can see that the baseline capacity at 1/2C remains unchanged after cycling at 2C. During cycling at 4C however, the electrode incurs additional damage and we can see another significant drop in the baseline 1/2C capacity of the electrode after cycling at this rate. This is confirmed by the observations in Fig. 6d, where we see visually that additional particles have become decohered. In contrast, no additional damage is incurred in the electrode during cycling at C-Rates of 1/4C and 1/10C, which are below the 1/2C baseline. As shown in Fig. 7, the baseline electrode capacity at 1/2C is recovered after intermittent cycling at lower C-Rates.

While use of a different statistical distribution for t_N^{cr} would clearly impact these results, the qualitative nature of the above study is nevertheless of significant importance and demonstrates: i) the importance of accounting for mechanical damage, which leads to a loss of electrochemical activity at the surface of an active particle, and ii) the manner in which that can be achieved computationally through use of the developed chemo-mechanical surface elements. In combination with further experimental calibration of material properties, the developed modeling technique should serve useful for analyzing the performance of future LIB electrode designs, including chemo-mechanical interactions and role of mechanical damage on electrochemical performance and capacity fade.

Modeling of Interfacial Damage in a LCO-LGPS Composite Cathode for an All-Solid-State Battery

We consider now an application of our modeling framework towards composite cathodes for all-solid-state batteries (SSBs) where active particles are connected through a relatively stiff solid-state electrolyte (SSE). The numerical investigation presented in the previous section demonstrated an example of a system where active particles in an electrode are chemically connected, but *mechanically isolated*. This section focuses specifically on a relevant engineering problem where active particles interact *both* through chemical connection and direct mechanical load transfer.

Common design of composite cathodes incorporates a densely packed architecture of active particles, confined on their exterior by a conductive matrix which supports percolation pathways for ionic transport in addition to complementary additives for electronic conduction.[29,64,65] The active material undergoes volumetric expansion/contraction during insertion/extraction of the ionic species,

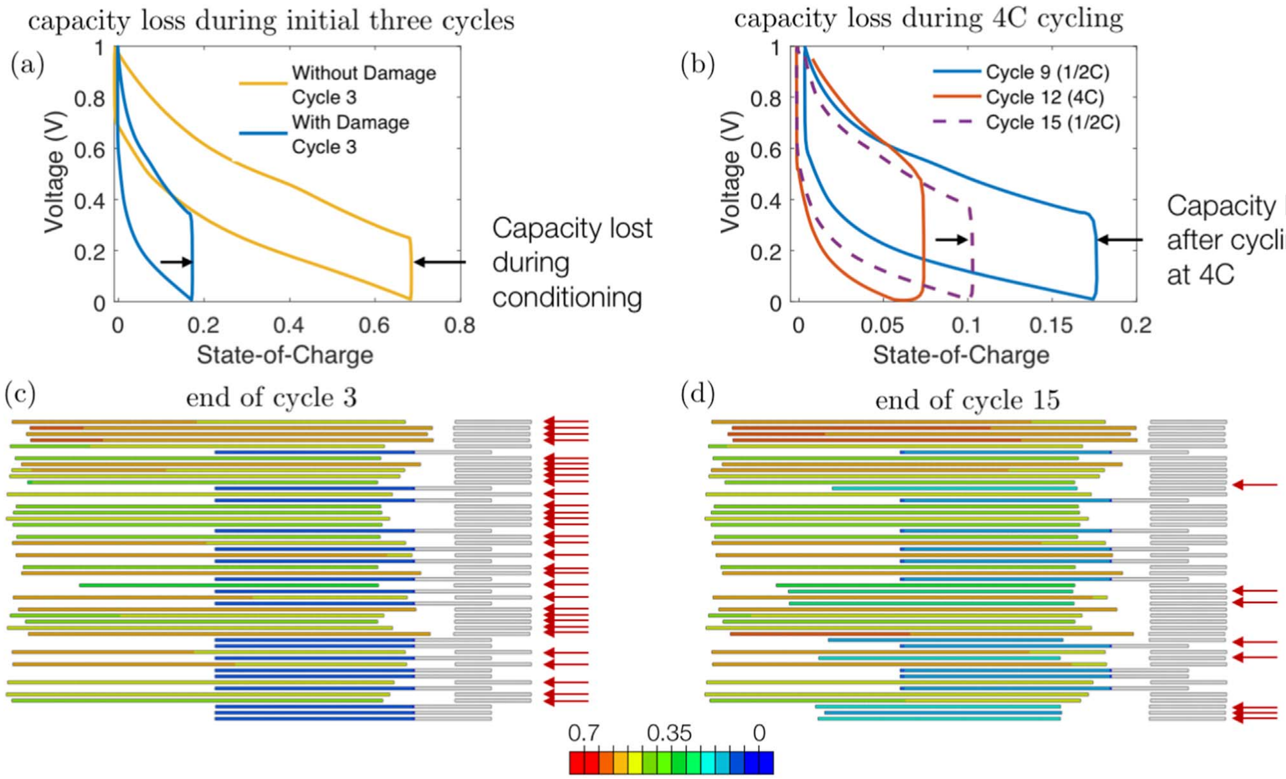

Figure 6. Simulation result of cycling a multi-particle electrode composed of double-walled, hollow nanotubes. Figures (a) and (b) show the Voltage vs SOC response of the electrode where (a) compares a simulation with and without damage after the first three conditioning cycles and (b) shows results of the simulation with damage after 9, 12, and 15 cycles. Figures (c) and (d) show contours of normalized concentration in the a-Si core at the end of the 3rd an 15th cycle. The red arrows highlight those particles which have completely decohered from their shells and are now chemically isolated.

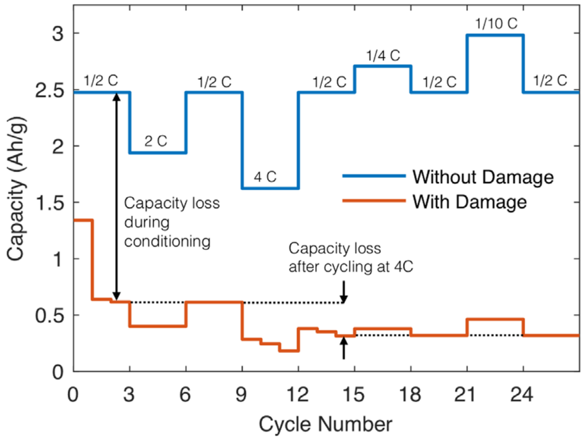

Figure 7. Capacity of an ensemble of hollow double-walled nanotubes as a function of cycle number during galvanostatic cycling at various C-rates. Results are shown for a simulation without interfacial damage (blue line) and a simulation with interfacial damage (orange line).

which, due to the confined nature of the all-solid-state architecture can lead to generation of high stresses. Delamination of the interface between active particles and the SSE constitutes a critical mechanical degradation mechanism, which can impact electrochemical performance of composite cathodes and SSBs.[66] As a result, efforts aimed at optimizing the performance of composite cathodes for application in SSBs require an understanding of interfacial processes, including damage, occurring within the electrode.

In this section, we specialize our framework for a system composed of $LiCoO_2$ (LCO) active particles and a $Li_{10}GeP_2S_{12}$ (LGPS) electrolyte, and integrate our chemo-mechanical cohesive element to capture interfacial reaction kinetics and damage. We apply this framework towards studying the manner in which various material and design parameters affect the electrochemical performance of the system. In particular we: i) investigate the role of variations in chemo-mechanical properties of the active material and SSE (i.e. volumetric expansion, Young's modulus), and ii) investigate the role of variations in microstructural characteristics (i.e. particle size distribution, packing density).

Model parameters.—For clarity and completeness, we summarize here all material parameters utilized in our simulation framework for the LCO-LGPS composite cathode under investigation. Where possible, material parameters are taken directly from the literature. The remaining properties have been calibrated to experimental data and a summary of the calibration process is presented. Material properties for our simulation framework are shown in Table I along with their sources. In the following subsections, we briefly detail the manner in which material properties were chosen or calibrated.

Mechanical properties of LCO and LGPS.—The mechanical behavior of the LCO active particles is taken as *chemo-elastic* and modeled using the same framework described in the "Bulk Particle Behavior" section above, however here without any plastic deformation. The LGPS SSE is treated as a purely elastic solid. Mechanical properties of LCO have been investigated in multiple works.[67–71] However, past studies and modeling efforts have resorted to an isotropic assumption, thus neglecting variations in mechanical properties of Li_xCoO_2 with Li content and crystallographic orientations. Wu and Zhang[72] applied first-principle calculations in addition to ab-initio tensile tests to study anisotropic and Li concentration-dependent mechanical properties of Li_xCoO_2. Variation in elastic stiffness, shear and bulk modulus with Li content along two axes of anisotropy were reported. While our simulation framework does not

Table I. Material properties for modeling the coupled chemo-mechanical behavior of an LCO-LGPS composite cathode.

	Parameter	Value	Source
Chemical	D_0	$5.387{\cdot}10^{-15}$ m^2 s^{-1}	Wiedemann et al. (2013)
	$c_{\text{R,max}}$	51 555 mol m^{-3}	Ramadass et al. (2013)
	$\Omega \cdot c_{\text{R,max}}$	-2%	Reimers and Dahn (1992)
	$[a_2, a_3, a_4, a_5, a_6, a_7]/F$	[0.1447, 0.4629, −0.7643, 2.5326, −3.199, 1.2263] V	Fitted to Mizushima et al. (1980)
	U_0^θ	4.6 V	Fitted to Mizushima et al. (1980)
Reaction Kinetics	k_0	$9 \cdot 10^{-7}$ mol/(m^2 s)	Fitted to Zhang et al. (2007)
Elastic	E_{LGPS}	37.19 GPa	Wang et al. (2014)
	ν_{LGPS}	0.296	Wang et al. (2014)
	E_{LCO}	108.5–252 GPa	Wu and Zhang (2015)
	ν_{LCO}	0.22	Wu and Zhang (2015)
Interfacial Mechanical	t_N^{cr}	[150, 250] MPa	N/A
	G_N	[1, 1.75] J m^{-2}	N/A
	K_N	$5 \cdot 10^{12}$ MPa/m	N/A

account for anisotropic behavior of Li_xCoO_2 in a formal continuum treatment, the aforementioned findings of Wu and Zhang are incorporated in the model through a Voigt-Reuss-Hill homogenization scheme, as reported in Ref. 73. Here, a sixth-order polynomial fit is performed to capture the variation of Young's Modulus with Li content from $E = 108.5$ GPa for a pristine, unlithiated state to $E = 252$ GPa for a fully-lithiated state. We employ a constant Poisson ratio of $\nu = 0.22$ for LCO. This effectively enables us to capture the experimentally reported variation in shear modulus with Li content from $G = 41.71$ GPa for an unlithiated state to $G = 111.38$ GPa for a fully lithiated state. A plot of the polynomial fit for both Young's modulus and Shear modulus against experimental data by Wu and Zhang[72] is reported in Section B in the accompanying Supporting Information.

The mechanical behavior of the LGPS SSE is modeled under a linear-elastic framework. Several studies have investigated the elastic properties of LGPS through first-principle calculations.[74,75] In a subsequent section of this work, we vary the mechanical properties of the SSE to investigate the potential impact of changing the SSE composition on electrochemical performance of the electrode. We use LGPS in our baseline simulations and reported values by Wang et al.[74] are used with a Young's modulus of $E = 37.19$ GPa and a Poisson ratio of $\nu = 0.296$.

Chemical properties of LCO.—Following Di Leo et al.,[39] we model the chemo-mechanical behavior of the LiCoO_2 active particles through the framework summarized above. An important aspect of using this framework is calibrating the activity coefficient through a fitting of the open-circuit behavior of the active material. In the absence of mechanical stresses, using 20, one can relate the chemical potential of Li atoms at the electrode surface to a stress-free, open-circuit potential U^θ, according to the following relationship (cf. Bucci et al.[44])

$$U^\theta = -\frac{\mu}{F} = -\frac{\mu^0}{F} - \frac{RT}{F}\ln\left(\gamma\frac{\bar{c}}{1-\bar{c}}\right) \qquad [23]$$

where $\text{U}_0^\theta = -\mu_0/F$ defines a standard rest potential. Motivated by Verbrugge and Koch,[76] the concentration dependent activity coefficient γ, is given by the following polynomial representation

$$RT\,\ln(\gamma) = \sum_{n=2}^{N} a_n \cdot n \cdot \bar{c}^{(n-1)}. \qquad [24]$$

Using Eqs. 23 and 24, a least-square polynomial regression fit is performed to published open-circuit potential data by Mizushima et al.[77] for a Li_xCoO_2 compound against a Li-metal reference/counter electrode to determine the polynomial coefficients in 24. In this work, a seventh order polynomial representation is adopted to determine the a_n coefficients and U_0^θ with the calibrated values summarized in Table I. A plot of the polynomial fit against experimental open-circuit potential data is shown in Section B in the accompanying Supporting Information.

To model the diffusion process, a Li diffusion coefficient of $D_0 = 5.387 \cdot 10^{-15}$ m^2/s and a maximum molar concentration of Li in the host material of $c_{\text{R,max}} = 51555$ mol m^{-3} are used. These values match with estimates employed in previous modeling efforts for a similar electrode material by Wiedemann et al.[78] and Ramadass et al.[79] We note that there is a large variation in reported estimates for the diffusion coefficient of Li in Li_xCoO_2 electrodes, with values ranging from 10^{-13} to 10^{-16} m^2 s^{-1}.[80–82] The volumetric changes experienced with added Li content, that is the partial molar volume Ω, is quantified based on the experimental findings of Reimers and Dahn.[83] It is important to note that in contrast to other active materials, Li_xCoO_2 experiences a *contraction* upon Li insertion, with an approximately 2% contraction in volume reported upon lithiation to $\text{Li}_{0.9}$ CoO_2. Based on these experimental observations, we set the quantity $\bar{\Omega} = \Omega c_{\text{R,max}} = -2\%$, which controls the total volumetric change of active particles due to intercalation.

To model interfacial kinetics, we calibrate the reaction constant, k_0, to experimental charge-discharge curves for Li_xCoO_2 published by Zhang et al.[84] We do so by adjusting k_0 so that energy dissipation during a full cycle (evaluated as the area inside the Voltage vs SOC curve) matches with experimental measurements. The calibration procedure is repeated at both a C-Rate of C/7 and C/2.7 to ensure consistency in calibration at different charging rates. The calibrated reaction constant is $k_0 = 9 \cdot 10^{-7}$ mol/(m^2 s). A figure of our calibration against the experimental charge-discharge curves by Zhang et al.[84] at a C-Rate of C/2.7 is shown in Section B in the accompanying Supporting Information.

Interfacial properties.—To the authors knowledge, no prior data on interface strength has been reported for a LCO-LPGS composite cathode and in general experimentally measured interface properties within SSBs are scarcely available as pointed out in the review work of Zhang et al.[85] As such, in the numerical investigations in subsequent sections, we prescribe t_N^{cr} values over a certain range to provide a qualitative assessment on the effect of damage on performance of composite cathodes in SSBs.

Further, we note that we consider only *normal* decohesion at the interface (i.e. $\beta = 0$ in Eqs. 12 and 13, and $t_T^{\text{cr}} \to \infty$), since given the limited experimental data available, it is not necessary at this stage to include a complex, mixed-mode failure mechanism for the interface. In the simulation section below, we vary the cohesive strength between $t_N^{\text{cr}} = 150$ MPa and $t_N^{\text{cr}} = 250$ MPa. Additionally, in selecting the aforementioned cohesive strengths, an effective Young's Modulus to Cohesive Strength ratio, $E_{\text{SSE}}/t_N^{\text{cr}} \in [0, 500]$ is maintained, comparable to similar studies in the literature.[20] Fracture energies of $G_N = 1\ \mathrm{J\ m^{-2}}$ and $G_N = 1.75\ \mathrm{J\ m^{-2}}$ are prescribed for the two different cohesive strengths to maintain a similar normal separation at failure. These values are consistent with the recent modeling efforts of Bucci et al.[20] Stiffness of the interface is prescribed equal to $K = K_N = 5 \cdot 10^{12}$ MPa/m. Choice of a sufficiently high interfacial stiffness is important to preserve the correct mechanical behavior of the microstructure prior to damage initiation and eliminate the addition of artificial compliance. The stiffness K was determined by running multiple simulations with increasing values of K and analyzing the development of normal stresses at the interface until a sufficiently large stiffness value to match the stress state for a perfectly bonded interface was determined.

Finally, the current density at a point on the surface of a particle is damaged through the parameter D_{chem}, which is taken to evolve according to

$$D_{\mathrm{chem}} = 1 - \exp(-\kappa \cdot D_{\mathrm{mech}}) \qquad [25]$$

where D_{mech} is the mechanical damage, which evolves according to Equation 11, and $\kappa = 30$. To model abrupt conductivity losses associated with brittle fracture (cf. Bucci et al.[20]), while simultaneously alleviate numerical convergence issues associated with unstable crack propagation, here we employ a numerical technique in which mechanical damage response is taken as ductile, while chemical damage is of a brittle nature. For the value of $\kappa = 30$ chosen, at 15% mechanical damage, $D_{mech} = 0.15$, we have already achieved 99% loss of chemical conductivity, $D_{chem} = 0.99$. This eases numerical convergence significantly without a loss of the ability to capture sudden losses in chemical conductivity due to mechanical damage and unstable crack propagation.

Effect of varying chemo-mechanical properties on electrochemical performance of SSB composite cathodes.—To study the effect of variations in chemo-mechanical properties on electrochemical response of a composite cathode, we consider a two-dimensional microstructure. SEM images of a $LiCoO_2$-$Li_{10}GeP_2S_{12}$ composite cathode provided in the work of Zhang et al.[29] and shown in Fig. 8a were used to construct a representative microstructure model as shown in Fig. 8b. We model the electrode particles to be elliptical in shape and prescribe the distribution in particle major and minor axis to match the experimental SEM images. Similar particle dimensions for representative $LiCoO_2$ microstructures are also reported in the work of Wilson et al.[86]

Periodic displacement boundary conditions are prescribed, effectively treating the simulated microstructure as a representative volume element (RVE). The surface of each electrode particle has been discretized with chemo-mechanical surface elements marked by red contour lines in Fig. 8b. The particles are electro-chemically coupled by prescribing that voltage across the active particle surfaces remains a constant as described in the theoretical and numerical framework section above. The assumption of a uniform potential along particles surface is reasonable in the context of composite electrodes composed of solid-state electrolytes with high ionic conductivity, which is the case for LGPS simulated here. One must accordingly relax this assumption when studying the electrochemical response of composite electrodes employing solid-state electrolytes with low ionic conductivity and in turn model the physics of transport of ionic species across the electrolyte. In the theoretical framework description, we briefly comment that the proposed framework would still be useful in such a system with the addition of modeling the necessary physics of transport through the electrolyte. Finally, we note that other complex degradation mechanisms, such as for example the formation of unstable interphases at the active particle/SSE interfaces can affect both mechanical degradation and interfacial kinetics.[24] Treatment of these phenomena is beyond the scope of this work, where we consider the active particle/SSE interface to remain pristine and be affected only due to mechanical decohesion.

We consider first the role of varying the Young's modulus of the SSE. We vary the elastic modulus between $E_{\mathrm{SSE}} = 20$ GPa and $E_{\mathrm{SSE}} = 100$ GPa, representing different families of inorganic electrolytes, namely sulfides, lithium phosphorous oxynitrides, and garnets.[19,85] The microstructure is cyclically charged-discharged at a C-Rate of 0.5C for five half-cycles between voltage caps of 3.8–4.6V.[a]

First, we establish a baseline behavior by running simulations *without interfacial damage*. The results are shown in Fig. 9 where (a) shows the average normal interfacial stress τ_N^{avg} experienced in all active particles during charging, while (b) shows the overall Voltage vs SOC behavior for the composite cathode. As shown in Fig. 9a, there is a significant increase in interfacial normal stresses (and hence also bulk stresses experienced by the active particles) as

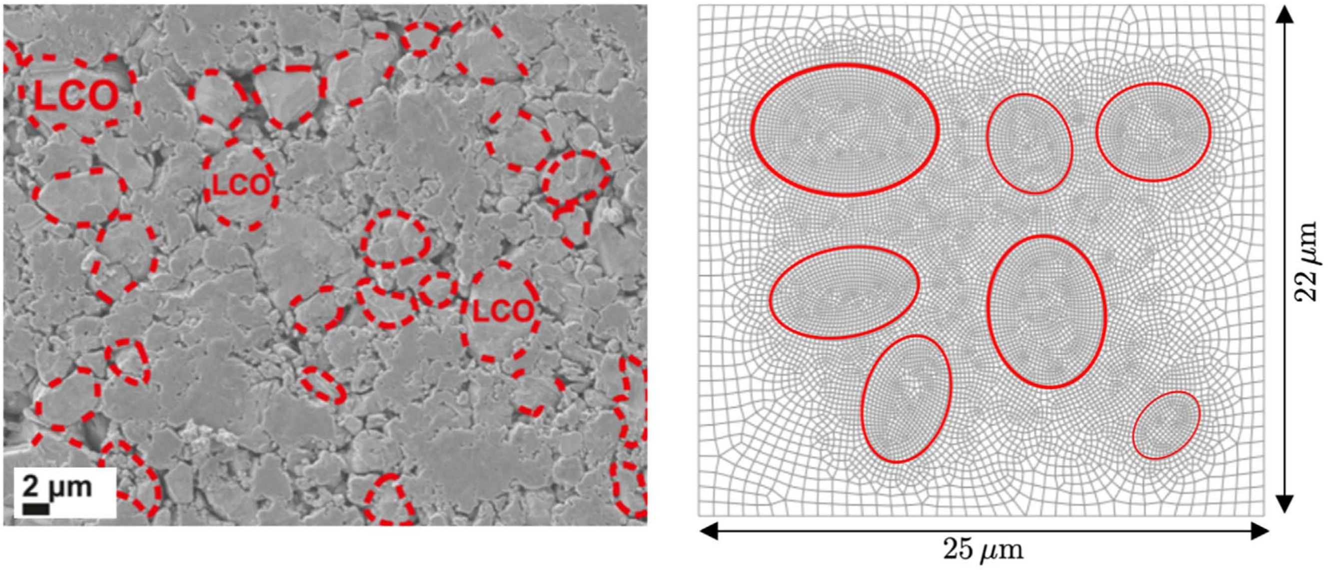

(a) (b)

Figure 8. (a) SEM image of a $LiCoO_2$-$Li_{10}GeP_2S_{12}$ composite cathode microstructure from the work of Zhang et al. Reprinted with permission from Ref. 29. (b) Graphical illustration of the 2D microstructure mimicking SEM images of Zhang et al.[29] used to model the effect of variation in chemo-mechanical properties on electrochemical performance of composite cathode.

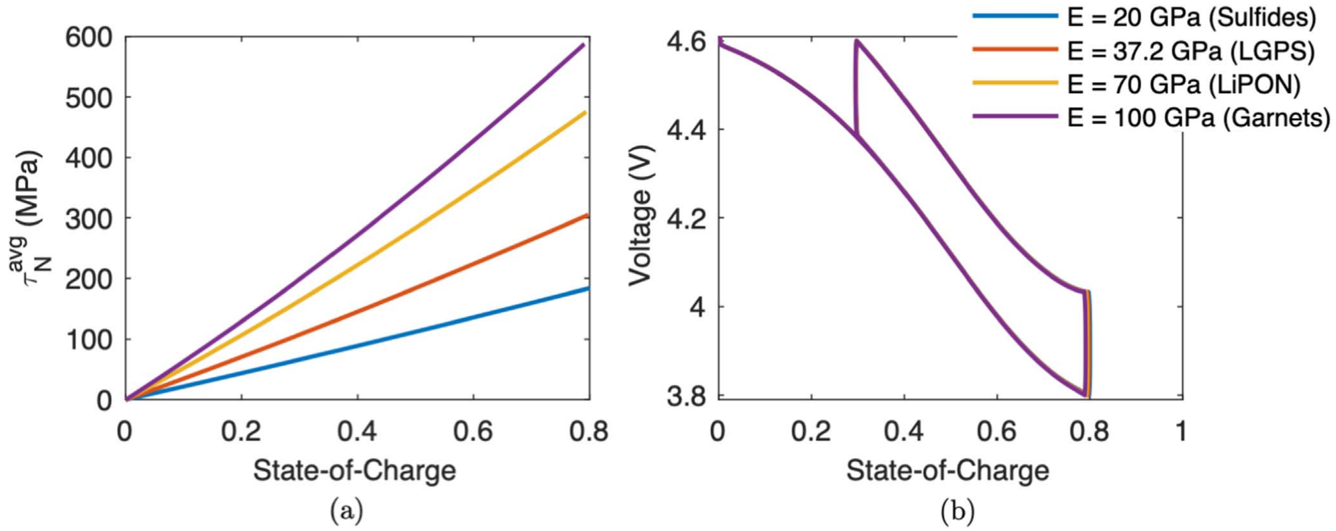

Figure 9. Composite cathode response with no damage and varying SSE Young's Modulus. (a) Average normal interfacial stress, τ_N^{avg} induced at the active-particle/SSE interface vs SOC. (b) Voltage vs SOC response of the composite electrode.

we increase the stiffness of the SSE. However, this increase in stress is not significant enough to in and of itself cause a significant change in electrochemical behavior of the composite cathode as shown in Fig. 9b. This increase in interfacial stresses can however have a significant impact on electrochemical performance if damage and decohesion of the interface is accounted for as shown next.

The electrochemical Voltage vs SOC response of the composite electrode with interfacial damage is shown in Fig. 10 with (a) $t_N^{cr} = 250$ MPa and (b) $t_N^{cr} = 150$ MPa for the baseline case of $\bar{\Omega} = -2\%$ volumetric contraction. For the relatively high stiffness in Fig. 10a, we see a decrease in electrochemical window (i.e. capacity) for all simulations with an SSE stiffness above 20 GPa. As expected, capacity fade becomes more pronounced with increase in SSE stiffness owing to the higher interfacial stress generation during deformation of the active particles. As these interfaces become damaged, they lose their current transfer capacity, which has two consequences. First, under galvanostatic charging, local current densities must increase to maintain a constant total current, leading to an increase in overpotential. Second, some particles may become disconnected from the SSE, making them inaccessible for further ion storage. The effect is further exacerbated at the lower interfacial strength of $t_N^{cr} = 150$ MPa shown in Fig. 10b, where we note a significant decrease in electrochemical window for all SSE stiffness values considered. These observations are consistent with previous modeling efforts by Bucci et al.[20] whereby compliant electrolytes are found to perform better at sustaining interfacial integrity.

We consider next the role of varying the volumetric change incurred by the $LiCoO_2$ active particles during lithiation and its effect on electrochemical performance. Here, we fix the normal interfacial strength at $t_N^{cr} = 250$ MPa. This mimics studying the potential effect of changing the composition of active particles to ones with higher capacity and hence higher volumetric changes during lithiation/delithiation. We consider a case with increased volumetric contraction upon lithiation with $\bar{\Omega} = -5\%$. The effect on the simulated voltage vs SOC response is shown by comparing Fig. 10a with $\bar{\Omega} = -2\%$ and (c) with $\bar{\Omega} = -5\%$. As observed by contrasting figures (a) and (c), increase in volumetric change upon lithiation of active particles has a drastic effect on the loss of electrochemical window due to mechanical interfacial damage. Specifically, in going from a low to a high stiffness SSE, capacity decreases by 56, 84, 90 and 95% when the volumetric contraction is 5%. In the extreme case where the SSE stiffness is $E_{\mathrm{SSE}} = 100$ GPa and the volumetric contraction is $\bar{\Omega} = -5\%$, the composite cathode loses almost its entire energy storing capacity as the majority of the particles in the electrode undergo complete decohesion from the SSE matrix. An animation of the simulations corresponding to Fig. 10 is shown in the Supplemental Video S3-SSB-Varying-Properties.mp4.

The results in Fig. 10 show a homogenized view of the composite cathode by describing the voltage vs SOC behavior of the entire simulation domain. Within the domain, there is a complex coupling in the manner in which mechanical stresses develop, damage occurs, and interfacial currents re-distribute. This coupling is illustrated in Fig. 11 for the simulation with $E_{\mathrm{SSE}} = 20$ GPa and $\bar{\Omega} = -5\%$. The top left image of Fig. 11 shows the average current density (blue), maximum interfacial normal stress τ_N^{max} (orange), and average damage (yellow) for "particle 1" which is labeled in Fig. 11a as the top-left particle in the simulation domain. Figs. 11a–11d show two sets of contours. Over the SSE domain we show the maximum in-plane principal stress σ_1, while in the active particles we show the normalized concentration $\bar{c}$. Note that deformations are scaled by a factor of 10 to better visualize the formation and evolution of interfacial decohesion. An animation of this simulation result can be found in the Supplemental Video S4-SSB-E20-O5.

Figure 11a shows a snapshot before any damage has occurred over the simulation domain (corresponding to the first dashed line in the top-left plot). At this point we can clearly see the formation of large stresses between particle pairs which are near each other. The remaining three contours shown in Figs. 11b through 11d show the progression of damage as the simulation evolves and the active particles lithiate. Critical to note is the behavior of Particle 1 as shown in the top-left corner. At time (b), we observe that Particle 1 experiences a change in the maximum normal traction it observes as well as the average current density over its surface. This is entirely due to crack formation at *other particles* in the simulation domain. This illustrates the complex mechanical and chemical coupling which occurs in solid-state composite cathodes. Interfacial damage in one particle, and the associated loss in current at the damage site, impacts *the mechanical behavior and interfacial current in all other particles in the domain*. The phenomena is again illustrated in Fig. 11c where further damage accumulated in the simulation domain—while Particle 1 remains undamaged—affects the interfacial behavior of Particle 1 as shown on the top-left image. Finally,

[a] From an experimental standpoint, Li_xCoO_2 is typically charged in the $0.5 \leqslant x \leqslant 1$ stoichiometric range to avoid the detrimental role of phase transitions on battery lifespan. In this work, however, we focus on understanding the role of mechanics and microstructural descriptors on electrochemical performance and neglect the role of phase transitions on capacity fade. As such, in our simulations, lithiation of Li_xCoO_2 particles from a pristine state is conducted. Studies employing a similar stoichiometric range are reported in the literature.[87–89] Additionally, doping techniques for mitigation of phase transitions in $LiCoO_2$ have been successful,[90] enabling for cycling at higher voltages.

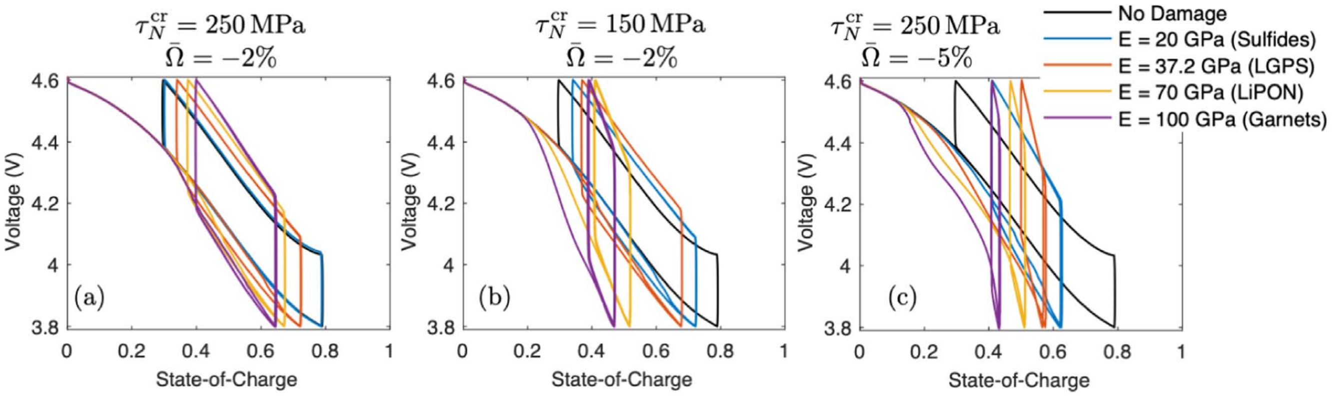

Figure 10. Effect of variations in SSE stiffness on electrochemical response of a composite cathode with different cohesive strengths t_N^{cr} and volumetric contractions of the active particles $\bar{\Omega}$. (a) Simulation results with high cohesive strength $t_N^{\mathrm{cr}} = 250$ MPa and 2% volumetric contraction, $\bar{\Omega} = -2\%$. (b) Results with reduced cohesive strength $t_N^{\mathrm{cr}} = 150$ MPa. (c) Results with increased 5% volumetric contraction, $\bar{\Omega} = -5\%$. The range of SSE stiffnesses considered are representative of Sulfides, LGPS, LiPON and Garnets.

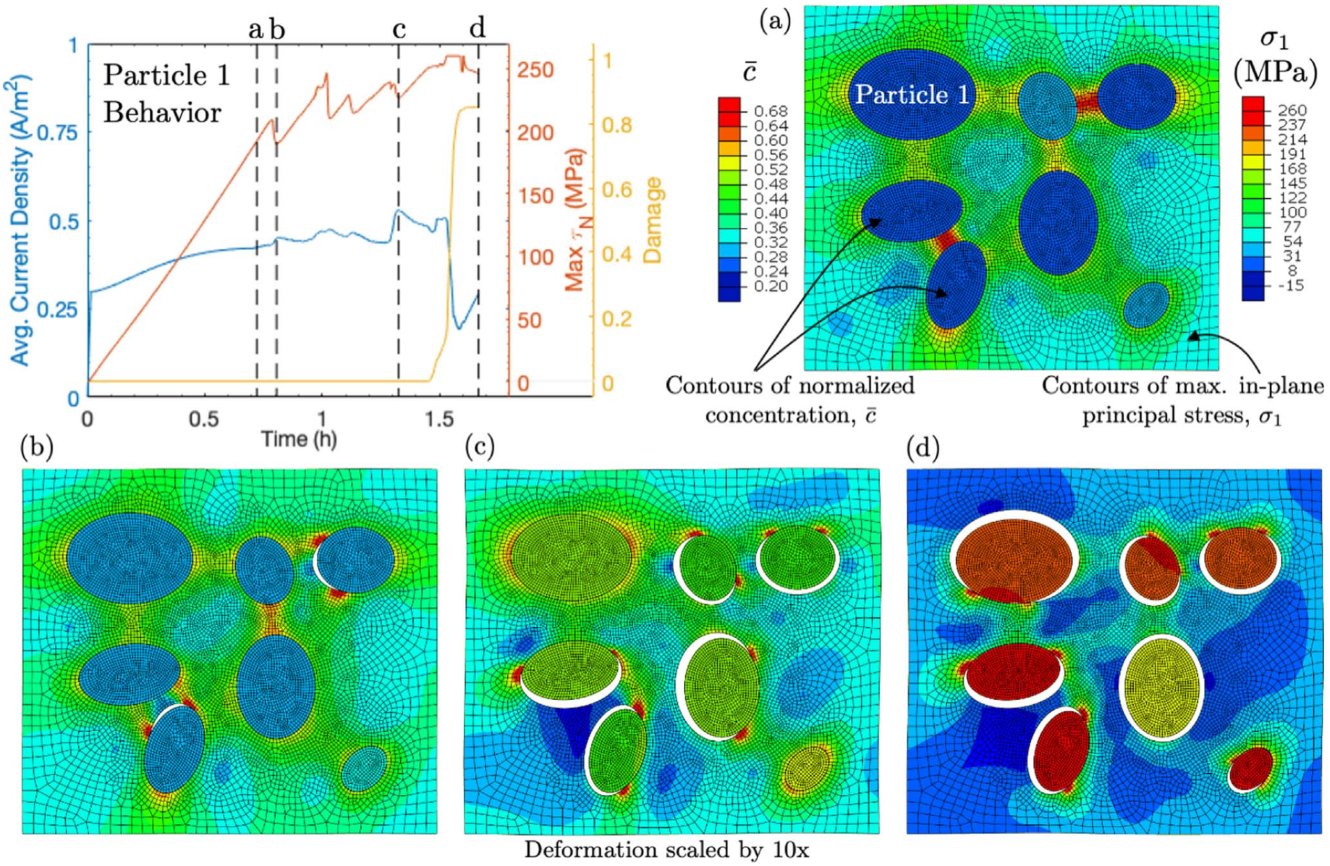

Figure 11. Simulation results for the particular case with $E_{SSE} = 20$ GPa and $\bar{\Omega} = -5\%$. The top-left plot shows the average current density, maximum normal interfacial stress $\tau_N^{\max}$, and average damage for Particle 1 which is shown in (a). Figures (a) through (d) show contours of maximum in-plane principal stress σ_1 in the SSE matrix, while contours of the normalized concentration $\bar{c}$ are shown over the active particles. Note that deformations are scaled by a factor of 10.

Fig. 11d shows the simulation domain at the end of the first half-cycle. Here, Particle 1 has incurred significant damage but remains partially connected to the SSE matrix.

Interfacial mechanical delamination is shown here to play a significant role in the manner in which SSE stiffness and choice of active material can affect electrochemical performance of all-solid-state composite electrodes. Even relatively small variations in these material properties can have a significant impact on electrochemical performance. From a design perspective, it is thus critical to map out design guidelines of material property pairs (such as SSE stiffness and active particle expansion/contraction) which will produce solid-state composite cathodes capable of sustaining integrity of the interface. This investigation also points out the critical need for further experiments to characterize the cohesive strength of different active particle/SSE interfaces as this can be critical to modeling the performance of composite electrodes.

Modeling the effect of particle size distribution and active material volume fraction on interface damage in composite cathodes.—We now turn our attention to studying the role of *microstructural descriptors* (e.g particle size distribution, packing density) on electrochemical performance and interfacial integrity of composite cathodes in SSBs. These studies provide insight into important design parameters of consideration for composite cathodes and further illustrate the use of the proposed numerical framework for modeling chemo-mechanical behavior of SSBs.

Role of particle size and size distribution on electrochemical performance and mechanical degradation.—We first study the effect of particle size distribution on electrochemical performance and mechanical degradation. As will be shown here, the key factor controlling the role of particle size distribution are *mechanical particle-particle interactions* arising from the presence of the relatively stiff SSE matrix, rather then the actual size (and size distribution) of the particles themselves. To illustrate this, we first conduct a simple study of an RVE composed of a single circular active particle embedded in the SSE matrix with periodic boundary conditions as shown in Fig. 12a. Note that *we do not allow for interfacial damage* in these single particle simulations and focus only on investigating the build up of mechanical stresses at the interface. Importantly, due to periodic boundary conditions, the simulated domain is a repeated RVE and does not represent a single mechanically isolated particle, but a repeating unit of particle pairs all of the same geometry. Using the simulation domain shown in Fig. 12a, we vary the volume fraction of active material defined through the geometric factor $f = R_{ap}/R_{ins}$ where R_{ap} is the active particle radius and R_{ins} is half the width of the simulation domain. The active material volume fraction is varied by changing both the particle size and the domain size through i) varying the active particle radius $R_{ap} \in [1,\ 10]\ \mu$m for a fixed domain size of $R_{ins} = 12.5\ \mu$m, and ii) varying the domain size $R_{ins} \in [6,\ 50]\ \mu$m for a constant active particle radius of $R_{ap} = 5\ \mu$m.

Figure 12b shows the average normal interfacial stress τ_N^{avg} induced in the particle at an SOC of 0.8 as a function of the active material volume fraction $f = R_{ap}/R_{ins}$. Results are shown both for simulations varying the active particle radius R_{ap} (circle markers) and simulations varying the domain size R_{ins} (x markers). The first critical observation to make is that the two simulation results are identical for a fixed active material volume fraction f. This demonstrates that active particle size by itself does not control stress generation at the interface, rather it is controlled by the active material volume fraction. In essence, form a design standpoint, generation of interfacial stresses is controlled by the electrode active material volume fraction (i.e. packing density)—through the presence of particle-particle mechanical interactions—and is *independent of the actual size of the active particles*. Similar results are found in the study by Bucci et al.[20]

The second critical observation shown in Fig. 12b is the importance of particle-particle interactions. At low active material volume fractions, roughly below $f = 0.3$, the particle simulated can be considered as "isolated" and we observe that the magnitude of τ_N^{avg} remains relatively constant and low. As volume fraction of active material increases, the particle (through the periodic boundary conditions) acts in a multi-particle behavior and is affected by particle-particle interactions. In this regime of higher volume fractions of active material, the magnitude of τ_N^{avg} increases rapidly with volume fraction as particle-particle interactions lead to a continuous increase in interfacial stresses as the spacing between particles is reduced.

We now expand our study beyond a single particle to investigate the performance of a composite cathode RVE with varying particle size distribution and constant volume fraction of active material. Figure 13 shows the simulated RVE domains, all of which have a constant active material volume fraction of $\phi_{AM} = 30\%$. Particle size and aspect ratio are seeded using a uniform distribution with prescribed lower and upper bounds. We consider active particle size bounds in the range of: i) 2–6 μm, ii) 4–5 μm, and iii) 6–7 μm. This allows us to investigate the response of the electrode for both a uniform distribution with relatively small (4–5 μm) and large particles (6–7 μm), as well as a distribution with a larger spread in particle sizes (2–6 μm). The RVEs were generated using MicrostructPy,[91] an open-source microstructure mesh generator, which allows the user to prescribe as an input the active material volume fraction and lower and upper bounds for the uniform distribution in particle size. The aspect ratio lower and upper bounds for the elliptical particles are set to 0.9 and 1.5 respectively for all simulation domains. We cycle the electrode over three half-cycles between 3.8–4.6 V voltage caps at a C-Rate of 1/2C *with interfacial damage active*. All material properties are as described in the previous section and for the interfacial cohesive strength we use $t_N^{cr} = 150$ MPa.

The Voltage vs SOC response of the three RVEs is shown in Fig. 14a and compared to simulation results with no damage (which are identical for all particle size distributions). As shown in Fig. 14a, electrochemical response of the RVE remains consistent across all RVEs with a fixed $\phi_{AM} = 30\%$, noting again that *particle size distribution is not a critical factor in determining electrochemical performance*.

The evolution of damage is also consistent across the three microstructures as shown in Figs. 14b and 14c. As noted in before, mechanical damage D_{mech} is taken to evolve in a rather ductile manner (so as to avoid numerical convergence issues), while chemical damage D_{chem}, defined in Equation 25, is of a brittle nature. Figure 14b shows the evolution of average D_{chem} (i.e average accumulated chemical damage) over the entire simulation domain as a function of time. We note that all damage occurs during the first charging half-cycle of the composite cathode and is fairly consistent across the various RVEs. During the second charging half-cycle, no additional damage occurs in any of the simulations and the electrode behavior stabilizes. In addition, Fig. 14c shows the evolution in Voltage as a function of the average D_{chem}. This figure can be useful to identify the manner in which adjusting the window of voltage limits in which we cycle the electrode will have a significant effect on accumulation of damage.

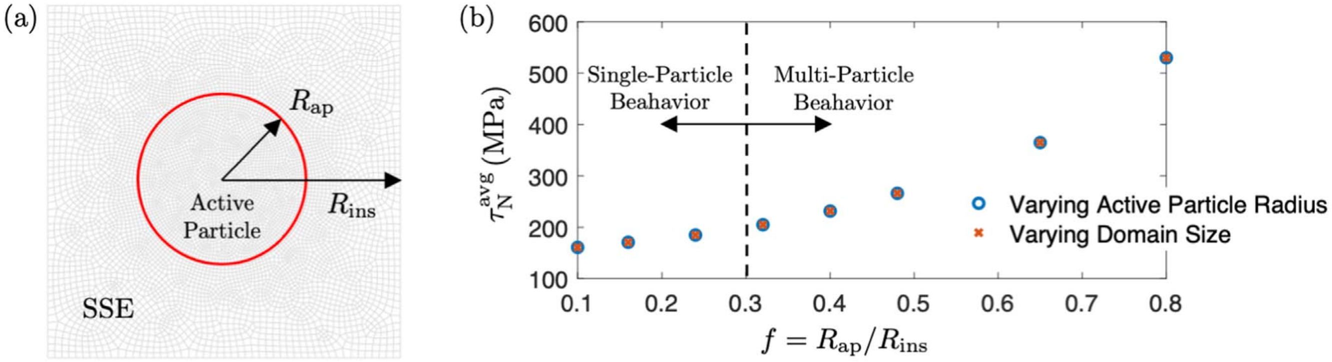

Figure 12. (a) Single particle representative volume element (RVE) simulation domain. (b) Plot of average normal interfacial stress τ_N^{avg} as a function of the geometric factor (i.e volume fraction) $f = R_{ap}/R_{ins}$.

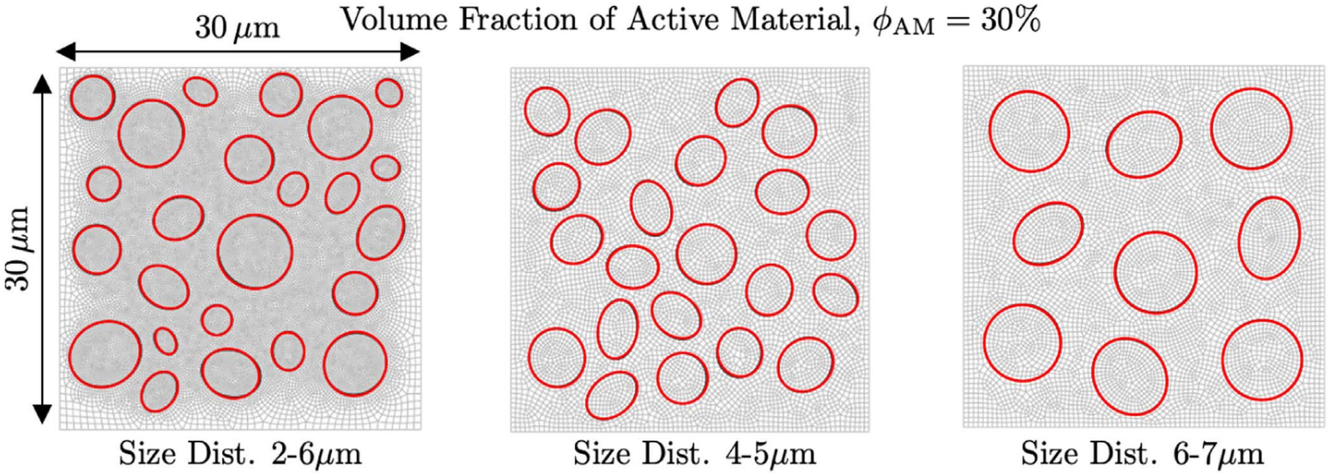

Figure 13. Simulated RVEs with a constant active material volume fraction $\phi_{\text{AM}} = 30\%$. The particle sizes are given a uniform distribution with lower and upper bounds in the range of: (i) 2–6 μm (ii) 4–5 μm and (iii) 6–7 μm. The aspect ratio lower and upper bounds fare set to 0.9 and 1.5 respectively for all cases.

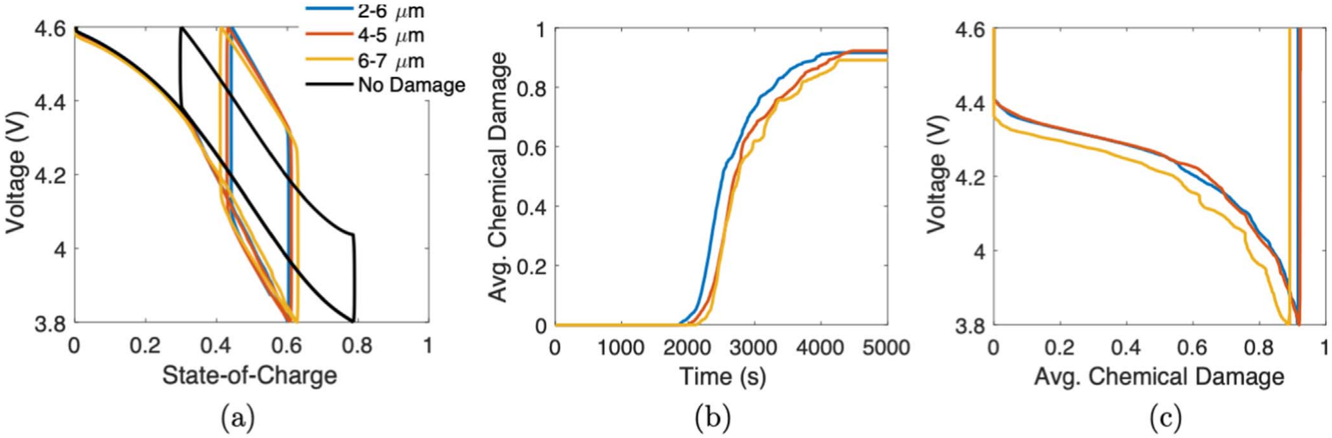

Figure 14. Simulation results for composite cathode RVEs with constant active material volume fraction $\phi_{\text{AM}} = 30\%$ and varying particle size distribution. (a) Voltage vs SOC behavior also compared to simulations with no damage. (b) Evolution of average D_{chem} as a function of time for the first half-cycle. (c) Evolution of Voltage as a function of average D_{chem}.

We note again that all RVEs have similar and consistent behaviors. Small differences in behavior of the three RVEs are related to the specific design of the microstructure, where for example, interactions between clusters of particles can lead to a slightly earlier initiation of damage. However, these differences are not significant as compared to changing the volume fraction of active material, as will be discussed in the next section.

Figure 15 shows the simulation domains at the end of the first half-cycle for the three RVEs, where in the active particles we show contours of the normalized concentration, $\bar{c}$, and in the SSE matrix we show contours of the maximum in-plane principal stress, σ_1. Note that deformation is scaled by 10× to best visualize interfacial degradation. We observe that damage is consistently distributed across all particles, irrespective of particle size, and that we sustain similar levels of stress in the matrix across all simulation domains. An animation of these simulations can be found in the Supplementary Movie S5-SSB-SizeDist. Finally, these results also hold for microstructure compositions with other active material volume fractions. We refer the reader to Section C in the Supporting Information for simulation results with $\phi_{\text{AM}} = 20\%$.

In this section, we have demonstrated that starting with a fixed composition of active material volume fraction, *variations in particle size and particle size distribution do not play a significant role in the build up of stress, subsequent damage, and ultimately on electrochemical performance*. From a design standpoint, this finding has important implications as it clearly points to the fact that reducing active particle size is not an effective mechanism for reducing interfacial stresses and damage. We next discuss the role of varying the active material volume fraction, ϕ_{AM}, which as expected from the discussion surrounding the results shown in Fig. 12, can have a significant effect.

Role of active material volume fraction on electrochemical performance and mechanical degradation.—We consider next the role of varying the *active material volume fraction,* ϕ_{AM} on electrochemical performance of SSB composite cathodes. Increasing the amount of active material in composite cathodes can be viewed as beneficial for it improves the overall volumetric capacity of the electrode. However, as demonstrated here, increasing the active material volume fraction can also lead to enhanced stress build up at the active particle/SSE interface, which can compromise mechanical integrity. This trade off poses the important question of whether there is a *critical active material volume fraction* which maximizes volumetric capacity in the presence of mechanical degradation at the active particle interfaces.

We consider four representative microstructures with active material volume fraction in the range $\phi_{\text{AM}} \in [20\%, 30\%, 40\%, 50\%]$ as shown in Fig. 16. Particle size distribution is the same for all simulation domains and is prescribed a uniform distribution with particle size lower and upper bounds at 2 and 6 μm respectively. As in the section above, the aspect ratio of active particles is also uniformly distributed with lower and upper bounds set at 0.9 and 1.5

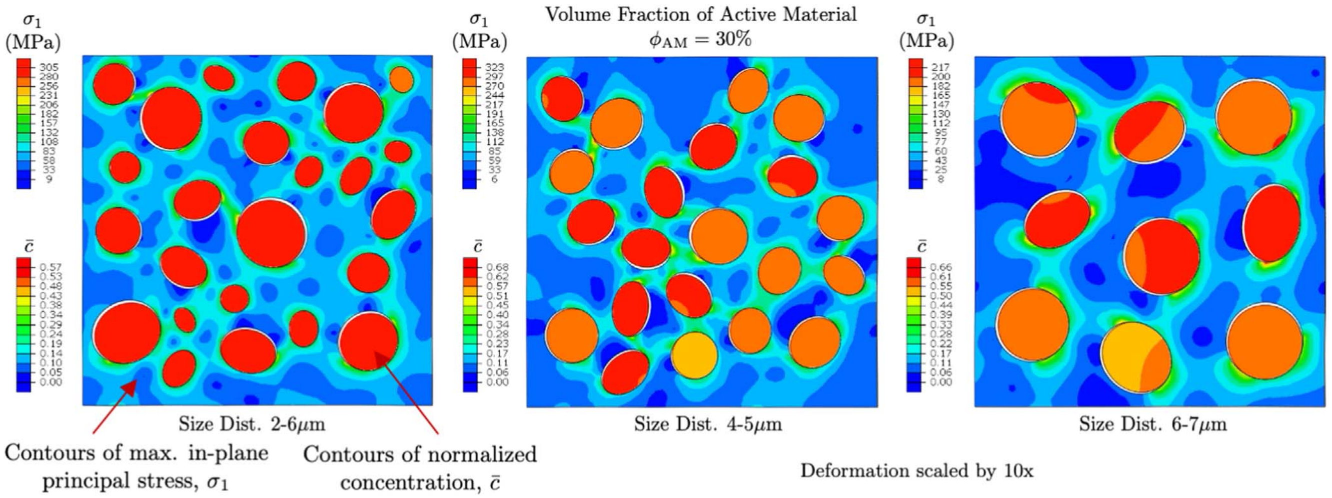

Figure 15. Simulation results for composite cathode RVEs with constant active material volume fraction $\phi_{\mathrm{AM}} = 30\%$ and varying particle size distribution. Results are shown at the end of the first half-cycle of each simulation domain.

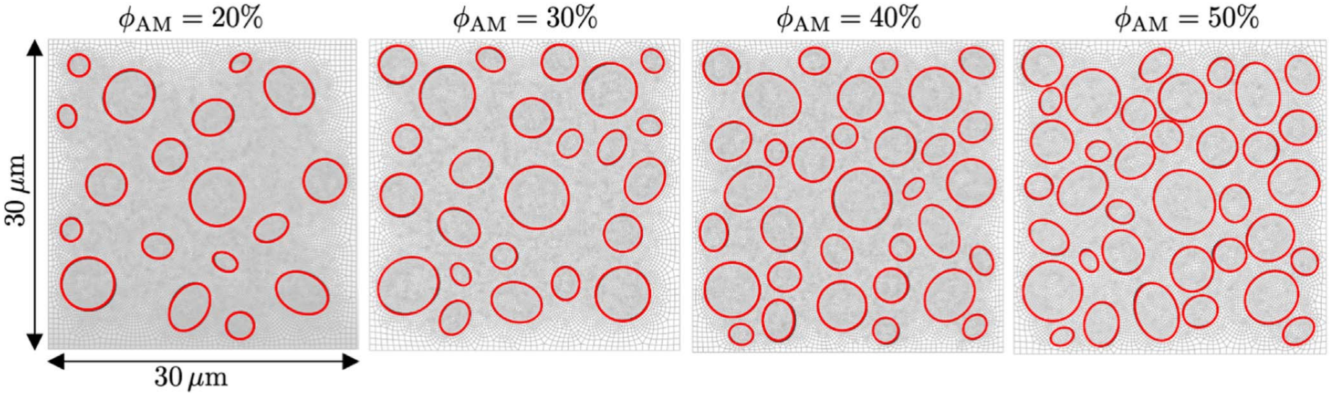

Figure 16. Simulated RVEs with a constant particle size distribution and varying active material volume fraction ϕ_{AM}.

respectively. This size distribution is chosen to match the experimental SEM image in the work of Zhang et al.[29] As before, boundary conditions are periodic and we cycle the electrode over three half-cycles between 3.8–4.6 V voltage caps at a constant C-Rate of 0.5C. Damage is modeled using the same material parameters described in the section above.

In order to account for an increase in capacity with added active material, we next present results plotted as a function of capacity computed with respect to the *total mass* of the electrode. Capacity here is thus computed as

$$\text{Capacity} = \frac{\int_{V_{\mathrm{AM}}} \bar{c}\, dV_{\mathrm{AM}} \cdot c_{\mathrm{R,max}} \cdot F}{m_{\mathrm{RVE}}} \qquad [26]$$

where m_{RVE} is the total mass of the composite cathode, $c_{\mathrm{R,max}}$ is the maximum molar concentration of the active material given in Table I, F is the Faraday constant, and $\bar{c}$ is the normalized concentration which in is integrated over the volume of active material. The mass of the RVE is computed as $m_{\mathrm{RVE}} = V_{AM} \cdot \rho_{AM} + V_{SSE} \cdot \rho_{SSE}$, with $\rho_{AM} = 4.79\ \mathrm{g\,cm^{-3}}$ for LCO as reported in Refs. 71, 92, while we determine the density of the SSE, $\rho_{SSE} = 2.1\ \mathrm{g\,cm^{-3}}$ from the work of Zhang et al.,[29] who reported both volume and mass ratios for various LCO-LGPS microstructure compositions.

Figures 17a and 17b show the Voltage vs Capacity curves for the four simulation domains with and without damage respectively. First, we note that as expected, simulations without damage, Fig. 17b, also show variations in Voltage vs Capacity response since capacity is normalized per total mass of the electrode. The effect of damage is clearly visible and we see a drastic change in electrochemical behavior when comparing Figs. 17a and 17b. In particular, we highlight the stable capacity as defined by the stable electrochemical window achieved following the first half-cycle. We can clearly observe that at a given volume fraction of active material, there is a drastic decrease in the stable capacity when damage is present.

The stable capacity is shown as a function of the active material volume fraction ϕ_{AM} in Fig. 17c. Here we plot the stable capacity for the undamaged (green line) and damaged (blue line) simulations. In addition we plot the difference of these two and label this as the capacity loss due to mechanical damage (red line). We observe here the manner in which active material volume fraction plays a critical role in electrochemical performance of the electrode in the presence of interfacial damage. Comparing the undamaged and damaged curves in Fig. 17c, we observe that as ϕ_{AM} is varied from 20% to 50%, stable capacity shrinks by 31, 46, 57, and 64 mAh $\mathrm{g^{-1}}$. In fact, one can observe that for simulations with damage in Fig. 17c, stable capacity remains nearly constant with ϕ_{AM}. This is due to the fact that capacity loss due to mechanical damage increases with ϕ_{AM} almost as rapidly as stable capacity of the undamaged microstructure increases with added active material. That is, *any capacity gains achieved by having a higher active volume fraction* ϕ_{AM} *are almost entirely negated by losses due to mechanical degradation.*

From a design perspective it is also useful to look at the Voltage vs accumulated chemical damage as shown in Fig. 17d. Two important trends can be observed here. First, damage *initiates*

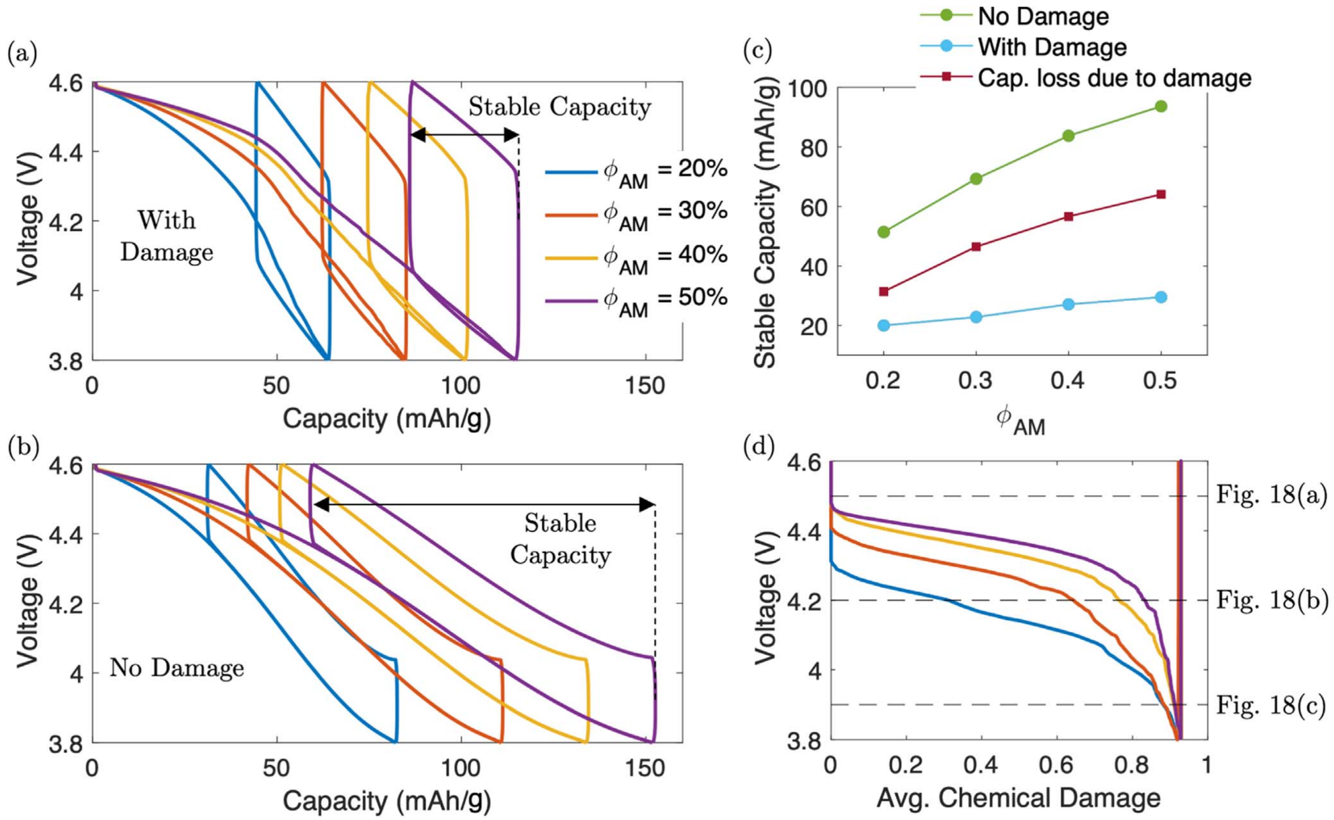

Figure 17. Simulation results for composite cathode RVEs with constant particle size distribution and varying volume fraction ϕ_{AM}. (a) and (b) show Voltage vs Capacity (defined per unit total mass of the RVE) for simulations with and without interfacial damage respectively. (c) Stable capacity during cycling as a function of ϕ_{AM} for simulations with and without damage and also shows the stable capacity loss due to damage, which is the difference of the two simulation results. (d) Voltage as a function of accumulated chemical damage (i.e. average D_{chem} in the entire simulation domain) for simulations with varying ϕ_{AM} and interfacial damage. Note the legend in (a) applies equally to (b) and (d).

earlier (i.e. at higher voltages) for microstructures with higher ϕ_{AM}. Second, the *rate of damage evolution* (i.e. the slope of the curve at intermediate accumulated chemical damage values) is also higher for microstructures with higher ϕ_{AM}. From a design standpoint, the data shown in Fig. 17d is also useful in allowing one to determine where a voltage cutoff could be placed in order to reduce damage. For example, at a voltage cutoff of 4.1 Volts, the microstructure with $\phi_{\mathrm{AM}} = 20\%$ will have only incurred approximately 60% accumulated damage as compared to 90% for microstructures with $\phi_{\mathrm{AM}} = 50\%$.

The detailed evolution of stresses, concentration, and damage are shown in Fig. 18, where we show results at (a) Voltage of 4.5 V (top row), (b) Voltage of 4.2 V (middle row), and (c) Voltage of 3.9 V (bottom row). The corresponding voltages are marked in Fig. 17d. In all results, we show contours of the maximum in-plane principal stress, σ_1 over the SSE matrix, and contours of normalized concentration, $\bar{c}$ over the active particles. In Fig. 18a, at 4.5 V, no damage has yet occurred over the domain (see Fig. 17d) and we can clearly observe the manner in which stresses increase with increase in ϕ_{AM}. We can also clearly observe how σ_1 hotspots arise between nearby particles due to mechanical particle-particle interactions. This trend persists at all voltages. In Fig. 18b, at 4.2 V, damage has initiated in all microstructures with significantly more damage occurring at higher ϕ_{AM}. A similar response is also observed at 3.9V in Fig. 18c.

Another important observation is with respect to the distribution of normalized concentration $\bar{c}$. Focusing on the results in Fig. 18c at 3.9 V, we can clearly observe that the *concentration of Li is more uniformly distributed over all particles in microstructures with small active material volume fraction* ϕ_{AM}. In contrast, simulations with high ϕ_{AM} show a broad range of concentrations over the various particles. This phenomena arises from the presence of mechanical interfacial damage. For simulations with high ϕ_{AM}, multiple particles have entirely decohered from the surrounding SSE matrix and thus have chemically isolated. These particles can no longer store Li ions and contribute to the overall loss of capacity due to mechanical damage experienced by the microstructures with higher active material volume fraction.

Concluding Remarks

We formulated and numerically implemented a theoretical framework based on the use of a chemo-mechanical surface element for modeling the stress-coupled, chemo-mechanical interactions in complex electrode designs under galvanostatic charging. In particular, the theoretical framework allows one to capture both chemical and mechanical interactions between active particles in battery electrodes. Under galvanostatic charging conditions, the theoretical framework captures chemical interactions between particles whereby current is distributed non-uniformly between active particles based on their local, stress-coupled interface reaction kinetics. Mechanically, the surface elements developed allow one to capture the role of mechanical interfacial damage on electrochemical performance by coupling interfacial current to mechanical damage. This allows one to model how loss of mechanical integrity at the interface limits transport kinetics and overall electrochemical performance of the electrode. We applied the theoretical framework to investigate the chemo-mechanical behavior—including interfacial degradation—of various composite electrodes under galvanostatic charging, with a focus on understanding how microstructural features such as local material properties, particle size distribution and packing density affect the overall electrochemical behavior of the composite electrode.

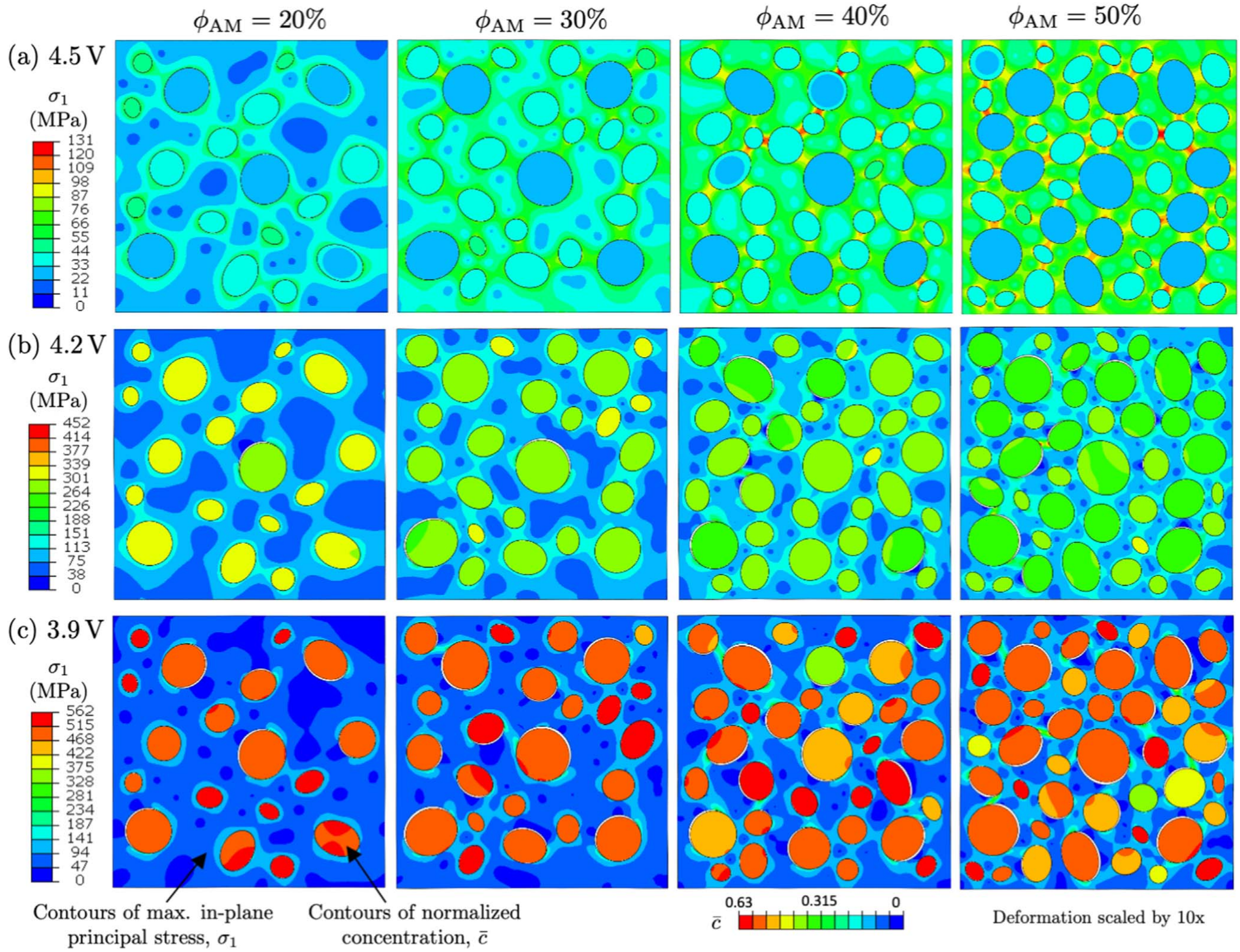

Figure 18. Simulation results for composite cathode RVEs with constant particle size distribution and varying volume fraction ϕ_{AM}. Results are shown at (a) Voltage of 4.5 V (top row), (b) Voltage of 4.2 V (middle row), and (c) Voltage of 3.9 V (bottom row). In all results, we show contours of the maximum in-plane principal stress, σ_1, over the SSE matrix, and contours of normalized concentration $\bar{c}$ over the active particles. Note that the colorbar for σ_1 is constant over a given Voltage, and the colorbar for $\bar{c}$ is constant for all simulations shown. Deformations are scaled by 10×.

We investigate the chemo-mechanical behavior of novel liquid LIB electrode designs composed of hollow a-Si nanotubes. This simulation represents a limiting case in a LIB electrode microstructure where particles are chemically connected, but mechanically isolated in the sense that there is no direct mechanical contact between particles. The following particular findings were made with respect to this electrode:

- The local reactivity, k_0 at the interface of individual particles was shown to play a critical role on the overall electro-chemical performance of the electrode. In particular, we demonstrated the manner in which sharp current transitions of the electrode, as seen in galvanostatic charging, are distributed unevenly with particles experiencing gradual variations in local current depending on their local reaction kinetics.
- The formation of stresses at the aSi/SiO_2 interfaces was investigated and it was observed that a decrease in C-Rate does not necessarily lead to a decrease in the maximum normal stresses experienced at the interface. This was investigated to arise from a combination of stresses induced by the degree of lithiation and strain-rate sensitivity of the material.
- Electrode capacity loss due to interfacial decohesion (i.e mechanical degradation) was investigated by performing a series of charge/discharge cycles at varying C-Rates. With the particular choice of material properties considered, we demonstrated the potential for large amounts of capacity loss due to mechanical degradation, with 75% loss of capacity observed during the first three conditioning cycles of the electrode.
- We demonstrated the manner in which the theoretical framework proposed can be used capture mechanically induced, electrochemical capacity loss over a number of different charging cycles. This is particularly important for assessing long-term electrode performance under different operation conditions.

We subsequently studied the chemo-mechanical behavior and electrochemical performance of a $LiCoO_2$-$Li_{10}GeP_2S_{12}$ composite cathode for all-solid-sate batteries. This set of simulations represents a typical all-solid-sate electrode microstructure where particles interact *both chemically and mechanically* through the galvanostatic charging constraint and stress transfer through the relatively stiff solid-state electrolyte. Material properties of electrode constituents were determined from the literature where available or fitted to available experimental results. The theoretical framework was then used to study three critical features of the microstructure. First, we studied the role of varying the chemo-mechanical properties of the composite electrode with a focus on the stiffness of the SSE and the volumetric contraction of active material. Second, we investigated the role of two critical microstructural features: i) the size and size distribution of active particles, and ii) the active material volume fraction (i.e. packing density). The following important findings were made with respect to this electrode:

- We demonstrated that variations in SSE stiffness and active material contraction during lithiation can have a large impact on electrochemical performance of SSB cathodes in the presence of interfacial delamination. The theoretical framework developed thus provides an important tool for future exploration of design of composite electrodes with different active material-SSE pairs in order to enhance mechanical integrity and concurrently electrochemical performance.
- With respect to microstructural composition, we first demonstrated that particle size does not play a critical role in stress build up at the interface and subsequent mechanical degradation. This was demonstrated both through simple, single-particle RVEs and through complex, multi-particle RVEs with different particle size distributions.
- The active material volume fraction was demonstrated to be a critical factor in electrochemical performance in the presence of mechanical degradation. This microstructural descriptor largely dictates the build up of interfacial stresses between the active material and SSE, and thus controls the onset and evolution of mechanical interfacial degradation.
- We demonstrated that while increasing active material volume fraction does naturally increase the capacity of the LCO-LGPS cathode under consideration, these gains can be quickly undermined by the enhanced mechanical interfacial degradation experienced. The theoretical framework developed provided a quantitative analysis of the manner in which capacity of a given RVE varies with increase in active material in the presence of mechanical interfacial degradation and can serve as a useful tool for design of complex, novel SSB cathode architectures for future applications.

Design of composite electrodes for optimal electrochemical performance in both LIBs and SSBs is a complex process, requiring an understanding of the chemo-mechanical, multi-particle interactions occurring at the electrode microstructure level. The theoretical framework developed builds upon our current, well-defined understanding of single-particle, chemo-mechanical constitutive models to provide a modeling technique for addressing microstructural behaviors, including the presence of mechanical interfacial damage and concurrent loss in reactivity at these interfaces. Further, the framework allows for accurate modeling of galvanostatic conditions and the concurrent non-uniform distribution of current across active particles based on their local, stress-coupled interface reaction kinetics. The framework is based on the use of a novel, chemo-mechanical surface element, which discretizes the active material/electrolyte interfaces and captures both non-linear reaction kinetics and mechanical damage occurring at these interfaces.

Future applications of this work can include the discretization and modeling of more realistic, tomographically resolved, 3D microstructures to further increase the accuracy of the predicted results. Introducing additional degradation mechanisms such as the formation of unstable interphases at the active particle/SSE interface is also critical and will enable more accurate predictions. In addition, we have restricted ourselves here to focusing on interfacial mechanical degradation at the active particle/SSE interfaces. The role of mechanical degradation on electrochemical performance in future studies can be extended to include damage within the constituents themselves. This can be done through the use of the chemo-mechanical surface elements developed (cf. Bucci et al.[19]) or through other damage modeling techniques such as gradient damage models (cf. Klinsmann et al.[93]). In pursuit of active material-SSE pairs with improved electrochemical performance and minimal mechanical degradation, concurrent modeling of damage within bulk materials as well as interfaces would be ideal for identifying the best material candidates for future SSB designs.

Acknowledgments

C.V.D.L. acknowledges funding from the National Science Foundation under Award No. CMMI-1825132.

ORCID

Claudio V. Di Leo https://orcid.org/0000-0002-3410-6677

References

1. M. Armand and J.-M. Tarascon, “Building better batteries.” *Nature*, **451**, 652 (2008).
2. B. Scrosati and J. Garche, “Lithium batteries: status, prospects and future.” *Journal of Power Sources*, **195**, 2419 (2010).
3. D. L. Wood III, J. Li, and C. Daniel, “Prospects for reducing the processing cost of lithium ion batteries.” *Journal of Power Sources*, **275**, 234 (2015).
4. P. G. Bruce, S. A. Freunberger, L. J. Hardwick, and J.-M. Tarascon, “Li-o 2 and li-s batteries with high energy storage.” *Nat. Mater.*, **11**, 19 (2012).
5. X. Yao, D. Liu, C. Wang, P. Long, G. Peng, Y.-S. Hu, H. Li, L. Chen, and X. Xu, “High-energy all-solid-state lithium batteries with ultralong cycle life.” *Nano Lett.*, **16**, 7148 (2016).
6. Y. Zhu, X. He, and Y. Mo, “Origin of outstanding stability in the lithium solid electrolyte materials: insights from thermodynamic analyses based on first-principles calculations.” *ACS Applied Materials & Interfaces*, **7**, 23685 (2015).
7. W. D. Richards, L. J. Miara, Y. Wang, J. C. Kim, and G. Ceder, “Interface stability in solid-state batteries.” *Chemistry of Materials*, **28**, 266 (2016).
8. D. Bistri, A. Afshar, and C. V. Di Leo, “Modeling the chemo-mechanical behavior of all-solid-state batteries: a review.” *Meccanica*, **55**, 1-32 (2020).
9. V. A. Sethuraman, M. J. Chon, M. Shimshak, V. Srinivasan, and P. R. Guduru, “In situ measurements of stress evolution in silicon thin films during electrochemical lithiation and delithiation.” *Journal of Power Sources*, **195**, 5062 (2010).
10. L. Y. Beaulieu, K. W. Eberman, R. L. Turner, L. J. Krause, and J. R. Dahn, “Colossal reversible volume changes in lithium alloys.” *Electrochemical and Solid State Letters*, **4**, A137 (2001).
11. K. Zhao, W. L. Wang, J. Gregoire, M. Pharr, Z. Suo, J. J. Vlassak, and E. Kaxiras, “Lithium-assisted plastic deformation of silicon electrodes in lithium-ion batteries: a first-principles theoretical study.” *Nano Lett.*, **11**, 2962 (2011).
12. K. Zhao, M. Pharr, S. Cai, J. J. Vlassak, and Z. Suo, “Large plastic deformation in high-capacity lithium-ion batteries caused by charge and discharge.” *J. Am. Ceram. Soc.*, **94**, s226 (2011).
13. X. H. Liu, L. Zhong, S. Huang, S. X. Mao, T. Zhu, and J. Y. Huang, “Size-dependent fracture of silicon nanoparticles during lithiation.” *ACS Nano*, **6**, 1522 (2012).
14. M. T. McDowell, I. Ryu, S. W. Lee, C. Wang, W. D. Nix, and Y. Cui, “Studying the kinetics of crystalline silicon nanoparticle lithiation with in situ transmission electron microscopy.” *Adv. Mater.*, **24**, 6034 (2012).
15. M. Ebner, F. Marone, M. Stampanoni, and V. Wood, “Visualization and quantification of electrochemical and mechanical degradation in li ion batteries.” *Science*, **342**, 716 (2013).
16. K. Zhao, M. Pharr, L. Hartle, J. J. Vlassak, and Z. Suo, “Fracture and debonding in lithium-ion batteries with electrodes of hollow core-shell nanostructures.” *Journal of Power Sources*, **218**, 6 (2012).
17. S. W. Lee, M. T. McDowell, L. A. Berla, W. D. Nix, and Y. Cui, “Fracture of crystalline silicon nanopillars during electrochemical lithium insertion.” *Proceedings of the National Academy of Sciences*, **109**, 4080-4085 (2012).
18. G. Bucci, T. Swamy, S. Bishop, B. W. Sheldon, Y.-M. Chiang, and W. C. Carter, “The effect of stress on battery-electrode capacity.” *J. Electrochem. Soc.*, **164**, A645 (2017).
19. G. Bucci, T. Swamy, Y.-M. Chiang, and W. C. Carter, “Modeling of internal mechanical failure of all-solid-state batteries during electrochemical cycling, and implications for battery design.” *Journal of Materials Chemistry A*, **5**, 19422 (2017).
20. G. Bucci, B. Talamini, A. R. Balakrishna, Y.-M. Chiang, and W. C. Carter, “Mechanical instability of electrode-electrolyte interfaces in solid-state batteries.” *Phys. Rev. Mater.*, **2**, 105407 (2018).
21. Y. Ren, Y. Shen, Y. Lin, and C.-W. Nan, “Direct observation of lithium dendrites inside garnet-type lithium-ion solid electrolyte.” *Electrochemistry Communications*, **57**, 27 (2015).
22. F. Aguesse, W. Manalastas, L. Buannic, J. M. L. del Amo, G. Singh, A. Llordes, and J. Kilner, “Investigating the dendritic growth during full cell cycling of garnet electrolyte in direct contact with li metal.” *ACS Applied Materials & Interfaces*, **9**, 3808 (2017).
23. L. Porz, T. Swamy, B. W. Sheldon, D. Rettenwander, T. Frömling, H. L. Thaman, S. Berendts, R. Uecker, W. C. Carter, and Y.-M. Chiang, “Mechanism of lithium metal penetration through inorganic solid electrolytes.” *Adv. Energy Mater.*, **7**, 1701003 (2017).
24. J. Tippens, J. C. Miers, A. Afshar, J. A. Lewis, F. J. Q. Cortes, H. Qiao, T. S. Marchese, C. V. Di Leo, C. Saldana, and M. T. McDowell, “Visualizing chemomechanical degradation of a solid-state battery electrolyte.” *ACS Energy Lett.*, **4**, 1475 (2019).
25. J. A. Lewis, F. J. Q. Cortes, M. G. Boebinger, J. Tippens, T. S. Marchese, N. Kondekar, X. Liu, M. Chi, and M. T. McDowell, “Interphase morphology between a solid-state electrolyte and lithium controls cell failure.” *ACS Energy Lett.*, **4**, 591 (2019).

26. H. Yang, W. Liang, X. Guo, C.-M. Wang, and S. Zhang, "Strong kinetics-stress coupling in lithiation of si and ge anodes." *Extreme Mechanics Letters*, **2**, 1 (2015).
27. R. Xu and K. Zhao, "Mechanical interactions regulated kinetics and morphology of composite electrodes in li-ion batteries." *Extreme Mechanics Letters*, **8**, 13 (2016), Nanomechanics: Bridging Spatial and Temporal Scales.
28. R. Xu, L. S. de Vasconcelos, and K. Zhao, "Computational analysis of chemo-mechanical behaviors of composite electrodes in li-ion batteries." *J. Mater. Res.*, **31**, 2715 (2016).
29. W. Zhang et al., "Interfacial processes and influence of composite cathode microstructure controlling the performance of all-solid-state lithium batteries." *ACS Applied Materials & Interfaces*, **9**, 17835 (2017).
30. Y. Zhao, P. Stein, Y. Bai, M. Al-Siraj, Y. Yang, and B.-X. Xu, "A review on modeling of electro-chemo-mechanics in lithium-ion batteries." *Journal of Power Sources*, **413**, 259 (2019).
31. J. Christensen and J. Newman, "A mathematical model of stress generation and fracture in lithium manganese oxide." *J. Electrochem. Soc.*, **153**, A1019 (2006).
32. J. Christensen and J. Newman, "Stress generation and fracture in lithium insertion materials." *Journal of Solid State Electrochemistry*, **10**, 293 (2006).
33. X. Zhang, W. Shyy, and A. M. Sastry, "Numerical simulation of intercalation-induced stress in li-ion battery electrode particles." *J. Electrochem. Soc.*, **154**, A910 (2007).
34. Y.-T. Cheng and M. W. Verbrugge, "The influence of surface mechanics on diffusion induced stresses within spherical nanoparticles." *J. Appl. Phys.*, **104**, 083521 (2008).
35. C. V. Di Leo, E. Rejovitzky, and L. Anand, "A cahn-hilliard-type phase-field theory for species diffusion coupled with large elastic deformations: application to phase-separating li-ion electrode materials." *Journal of the Mechanics and Physics of Solids*, **70**, 1 (2014).
36. R. Purkayastha and R. McMeeking, "Stress due to the intercalation of lithium in cubic-shaped particles: a parameter study." *Meccanica*, **51**, 3081 (2016).
37. Z. Cui, F. Gao, and J. Qu, "A finite deformation stress-dependent chemical potential and its applications to lithium ion batteries." *Journal of the Mechanics and Physics of Solids*, **60**, 1280 (2012).
38. M. G. Boebinger et al., "Avoiding fracture in a conversion battery material through reaction with larger ions." *Joule*, **2**, 1783 (2018).
39. C. V. Di Leo, E. Rejovitzky, and L. Anand, "Diffusion deformation theory for amorphous silicon anodes: the role of plastic deformation on electrochemical performance." *International Journal of Solids and Structures*, **67–68**, 283 (2015).
40. A. F. Bower, P. R. Guduru, and V. A. Sethuraman, "A finite strain model of stress, diffusion, plastic flow, and electrochemical reactions in a lithium-ion half-cell." *Journal of the Mechanics and Physics of Solids*, **59**, 804 (2011).
41. A. F. Bower and P. R. Guduru, "A simple finite element model of diffusion, finite deformation, plasticity and fracture in lithium ion insertion electrode materials." *Model. Simul. Mater. Sci. Eng.*, **20**, 045004 (2012).
42. L. Anand, "A cahn-hilliard-type theory for species diffusion coupled with large elastic-plastic deformations." *Journal of the Mechanics and Physics of Solids*, **60**, 1983 (2012).
43. K. Zhao, M. Pharr, Q. Wan, W. L. Wang, E. Kaxiras, J. J. Vlassak, and Z. Suo, "Concurrent reaction and plasticity during initial lithiation of crystalline silicon in lithium-ion batteries." *J. Electrochem. Soc.*, **159**, A238 (2011).
44. G. Bucci, S. P. V. Nadimpalli, V. A. Sethuraman, A. F. Bower, and P. R. Guduru, "Measurement and modeling of the mechanical and electrochemical response of amorphous si thin film electrodes during cyclic lithiation." *Journal of the Mechanics and Physics of Solids*, **62**, 276 (2014).
45. H. Wu et al., "Stable cycling of double-walled silicon nanotube battery anodes through solid-electrolyte interphase control." *Nat. Nanotechnol.*, **7**, 310 (2012).
46. S. W. Lee, H.-W. Lee, I. Ryu, W. D. Nix, H. Gao, and Y. Cui, "Kinetics and fracture resistance of lithiated silicon nanostructure pairs controlled by their mechanical interaction." *Nat. Commun.*, **6**, 7533 (2015).
47. E. K. Rahani and V. B. Shenoy, "Role of plastic deformation of binder on stress evolution during charging and discharging in lithium-ion battery negative electrodes." *J. Electrochem. Soc.*, **160**, A1153 (2013).
48. K. Higa and V. Srinivasan, "Stress and strain in silicon electrode models." *J. Electrochem. Soc.*, **162**, A1111 (2015).
49. E. García, Y. M. Chiang, W. Carter, P. Limthongkul, and C. M. Bishop, "Microstructural modeling and design of rechargeable lithium-ion batteries." *J. Electrochem. Soc.*, **152**, A255 (2005).
50. R. Xu, Y. Yang, F. Yin, P. Liu, P. Cloetens, Y. Liu, F. Lin, and K. Zhao, "Heterogeneous damage in li-ion batteries: experimental analysis and theoretical modeling." *Journal of the Mechanics and Physics of Solids*, **129**, 160 (2019).
51. R. Xu, L. S. De Vasconcelos, J. Shi, J. Li, and K. Zhao, "Disintegration of meatball electrodes for LiNixMnyCozO 2 cathode materials." *Experimental Mechanics*, **58**, 549 (2018).
52. T. Hofmann, D. Westhoff, J. Feinauer, H. Andrä, J. Zausch, V. Schmidt, and R. Müller, "Electro-chemo-mechanical simulation for lithium ion batteries across the scales." *International Journal of Solids and Structures*, **184**, 24 (2020).
53. R. Behrou and K. Maute, "Numerical modeling of damage evolution phenomenon in solid-state lithium-ion batteries." *J. Electrochem. Soc.*, **164**, A2573 (2017).
54. M. Al-Siraj, P. Stein, and B.-X. Xu, "The effect of morphology changes and mechanical stresses on the effective diffusivity of solid electrolyte for lithium ion batteries." *J. Electrochem. Soc.*, **167**, 020535 (2020).
55. M. Z. Bazant, "Theory of chemical kinetics and charge transfer based on nonequilibrium thermodynamics." *Acc. Chem. Res.*, **46**, 1144 (2013).
56. L. Chen, H. W. Zhang, L. Y. Liang, Z. Liu, Y. Qi, P. Lu, J. Chen, and L.-Q. Chen, "Modulation of dendritic patterns during electrodeposition: a nonlinear phase-field model." *Journal of Power Sources*, **300**, 376 (2015).
57. P. P. Camanho, C. G. Davila, and M. F. de Moura, "Numerical simulation of mixed-mode progressive delamination in composite materials." *Journal of Composite Materials*, **37**, 1415 (2003), 2019/08/10.
58. L. Hamitouche, M. Tarfaoui, and A. Vautrin, "An interface debonding law subject to viscous regularization for avoiding instability: application to the delamination problems." *Engineering Fracture Mechanics*, **75**, 3084 (2008).
59. C. V. Di Leo, "Chemo-mechanics of lithium-ion battery electrodes." *PhD Thesis*, Massachusetts Institute of Technology (2015), https://dspace.mit.edu/handle/1721.1/100119.
60. S. A. Chester, C. V. Di Leo, and L. Anand, "A finite element implementation of a coupled diffusion-deformation theory for elastomeric gels." *International Journal of Solids and Structures*, **52**, 1 (2015).
61. E. Rejovitzky, C. V. Di Leo, and L. Anand, "A theory and a simulation capability for the growth of a solid electrolyte interphase layer at an anode particle in a li-ion battery." *Journal of the Mechanics and Physics of Solids*, **78**, 210 (2015).
62. A. Mukhopadhyay, A. Tokranov, X. Xiao, and B. W. Sheldon, "Stress development due to surface processes in graphite electrodes for li-ion batteries: a first report." *Electrochimica Acta*, **66**, 28 (2012).
63. Y. M. Lee, J. Y. Lee, H.-T. Shim, J. K. Lee, and J.-K. Park, "SEI layer formation on amorphous si thin electrode during precycling." *J. Electrochem. Soc.*, **154**, A515 (2007).
64. A. Bielefeld, D. A. Weber, and J. Janek, "Microstructural modeling of composite cathodes for all-solid-state batteries." *The Journal of Physical Chemistry C*, **123**, 1626 (2018).
65. A. Bielefeld, D. A. Weber, and J. Janek, "Modeling effective ionic conductivity and binder influence in composite cathodes for all-solid-state batteries." *ACS Applied Materials & Interfaces*, **12**, 12821 (2020).
66. W. Zhang, F. H. Richter, S. P. Culver, T. Leichtweiss, J. G. Lozano, C. Dietrich, P. G. Bruce, W. G. Zeier, and J. Janek, "Degradation mechanisms at the Li10GeP2S12/LiCoO2 cathode interface in an all-solid-state lithium-ion battery." *ACS Applied Materials & Interfaces*, **10**, 22226 (2018).
67. F. X. Hart and J. B. Bates, "Lattice model calculation of the strain energy density and other properties of crystalline licoo 2." *J. Appl. Phys.*, **83**, 7560 (1998).
68. H. Wang, Y.-I. Jang, B. Huang, D. R. Sadoway, and Y.-M. Chiang, "Tem study of electrochemical cycling-induced damage and disorder in LiCoO2 cathodes for rechargeable lithium batteries." *J. Electrochem. Soc.*, **146**, 473 (1999).
69. M. Qu, W. H. Woodford, J. M. Maloney, W. Craig Carter, Y.-M. Chiang, and K. J. Van Vliet, "Nanomechanical quantification of elastic, plastic, and fracture properties of LiCoO2." *Adv. Energy Mater.*, **2**, 940 (2012).
70. Y. Qi, L. G. Hector, C. James, and K. J. Kim, "Lithium concentration dependent elastic properties of battery electrode materials from first principles calculations." *J. Electrochem. Soc.*, **161**, F3010 (2014).
71. E. J. Cheng, N. J. Taylor, J. Wolfenstine, and J. Sakamoto, "Elastic properties of lithium cobalt oxide (LiCoO2)." *Journal of Asian Ceramic Societies*, **5**, 113 (2017).
72. L. Wu and J. Zhang, "Ab initio study of anisotropic mechanical properties of LiCoO2 during lithium intercalation and deintercalation process." *J. Appl. Phys.*, **118**, 225101 (2015).
73. C.-S. Man and M. Huang, "A simple explicit formula for the voigt-reuss-hill average of elastic polycrystals with arbitrary crystal and texture symmetries." *Journal of Elasticity*, **105**, 29 (2011).
74. Z. Q. Wang, M. S. Wu, G. Liu, X. L. Lei, B. Xu, and C. Y. Ouyang, "Elastic properties of new solid state electrolyte material Li10GeP2S12: A study from first-principles calculations." *Int. J. Electrochem. Sci.*, **9**, 562-568 (2014).
75. Z. Deng, Z. Wang, I.-H. Chu, J. Luo, and S. P. Ong, "Elastic properties of alkali superionic conductor electrolytes from first principles calculations." *J. Electrochem. Soc.*, **163**, A67 (2016).
76. M. W. Verbrugge and B. J. Koch, "Modeling lithium intercalation of single-fiber carbon microelectrodes." *J. Electrochem. Soc.*, **143**, 600 (1996).
77. K. Mizushima, P. C. Jones, P. J. Wiseman, and J. B. Goodenough, "LixCoO2 ($0 < x < -1$): A new cathode material for batteries of high energy density." *Mater. Res. Bull.*, **15**, 783 (1980).
78. A. H. Wiedemann, G. M. Goldin, S. A. Barnett, H. Zhu, and R. J. Kee, "Effects of three-dimensional cathode microstructure on the performance of lithium-ion battery cathodes." *Electrochimica Acta*, **88**, 580 (2013).
79. P. Ramadass, B. Haran, R. White, and B. N. Popov, "Mathematical modeling of the capacity fade of li-ion cells." *Journal of Power Sources*, **123**, 230 (2003).
80. A. Honders, J. M. Der Kinderen, A. H. Van Heeren, J. H. W. De Wit, and G. H. J. Broers, "Bounded diffusion in solid solution electrode powder compacts. part ii. the simultaneous measurement of the chemical diffusion coefficient and the thermodynamic factor in lixtis2 and lixcoo2." *Solid State Ionics*, **15**, 265 (1985).
81. Y.-M. Choi, S.-I. Pyun, J.-S. Bae, and S.-I. Moon, "Effects of lithium content on the electrochemical lithium intercalation reaction into LiNiO2 and LiCoO2 electrodes." *Journal of Power Sources*, **56**, 25 (1995).
82. Y.-I. Jang, B. J. Neudecker, and N. J. Dudney, "Lithium diffusion in LixCoO2 ($0.45 < x < 0.7$) intercalation cathodes." *Electrochemical and Solid State Letters*, **4**, A74 (2001).
83. J. N. Reimers and J. R. Dahn, "Electrochemical and in situ x-ray diffraction studies of lithium intercalation in LixCoO2." *J. Electrochem. Soc.*, **139**, 2091 (1992).
84. Q. Zhang, Q. Guo, and R. E. White, "Semi-empirical modeling of charge and discharge profiles for a LiCoO2 electrode." *Journal of Power Sources*, **165**, 427 (2007).
85. F. Zhang, Q.-A. Huang, Z. Tang, A. Li, Q. Shao, L. Zhang, X. Li, and J. Zhang, "A review of mechanics-related material damages in all-solid-state batteries: mechanisms, performance impacts and mitigation strategies." *Nano Energy*, **70**, 104545 (2020).

86. J. R. Wilson, J. S. Cronin, S. A. Barnett, and S. J. Harris, “Measurement of three-dimensional microstructure in a licoo2 positive electrode.” *Journal of Power Sources*, **196**, 3443 (2011).
87. Y.-I. Jang, N. J. Dudney, D. A. Blom, and L. F. Allard, “Electrochemical and electron microscopic characterization of thin-film LiCoO2 cathodes under high-voltage cycling conditions.” *Journal of Power Sources*, **119**, 295 (2003).
88. H. Xia, S. Y. Meng, L. Lu, and G. Ceder, “Electrochemical behavior and li diffusion study of LiCoO2 thin film electrodes prepared by PLD.”*Advanced Materials for Micro- and Nano-Systems (AMMNS)* (2007).
89. Z. Chen, Z. Lu, and J. R. Dahn, “Staging phase transitions in LixCoO2.” *J. Electrochem. Soc.*, **149**, A1604 (2002).
90. Q. Liu et al., “Approaching the capacity limit of lithium cobalt oxide in lithium ion batteries via lanthanum and aluminium doping.” *Nat. Energy*, **3**, 936 (2018).
91. K. A. Hart and J. J. Rimoli, “Microstructpy: a statistical microstructure mesh generator in python.” *SoftwareX*, **12**, 100595 (2020).
92. J. Akimoto, Y. Gotoh, and Y. Oosawa, “Synthesis and Structure Refinement of LiCoO2 Ssingle Crystals.” *Journal of Solid State Chemistry*, **141**, 298-302 (1998).
93. M. Klinsmann, D. Rosato, M. Kamlah, and R. M. McMeeking, “Modeling crack growth during Li insertion in storage particles using a fracture phase field approach.” *Journal of the Mechanics and Physics of Solids*, **92**, 313-344 (2016).